

ΠΑΝΕΠΙΣΤΗΜΙΟ ΠΑΤΡΩΝ

ΤΜΗΜΑ ΙΑΤΡΙΚΗΣ ΤΜΗΜΑ ΦΥΣΙΚΗΣ

**ΔΙΑΤΜΗΜΑΤΙΚΟ ΠΡΟΓΡΑΜΜΑ
ΜΕΤΑΠΤΥΧΙΑΚΩΝ ΣΠΟΥΔΩΝ
ΣΤΗΝ
ΙΑΤΡΙΚΗ ΦΥΣΙΚΗ**



ΜΕΤΑΠΤΥΧΙΑΚΗ ΕΡΓΑΣΙΑ

**ΜΕΘΟΔΟΛΟΓΙΑ ΑΝΑΠΤΥΞΗΣ ΑΛΓΟΡΙΘΜΩΝ ΓΙΑ ΤΗΝ
ΕΠΕΞΕΡΓΑΣΙΑ ΚΑΙ ΑΝΑΛΥΣΗ ΕΙΚΟΝΩΝ ΤΟΜΟΓΡΑΦΙΑΣ
ΟΠΤΙΚΗΣ ΣΥΝΟΧΗΣ (O.C.T)**

ΜΑΝΔΕΛΙΑΣ ΚΩΝΣΤΑΝΤΙΝΟΣ

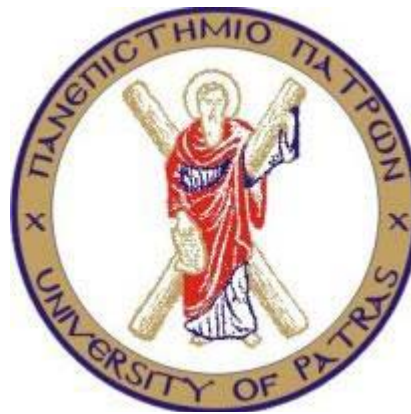
ΠΑΤΡΑ 2012

UNIVERSITY OF PATRAS

**School Of Health Sciences
Faculty Of Medicine**

**School Of Natural Sciences
Department Of Physics**

INTERDEPARTMENTAL POSTGRADUATE PROGRAM IN MEDICAL PHYSICS



MASTER THESIS

**METHODOLOGY DEVELOPMENT ALGORITHMS FOR
PROCESSING AND ANALYSIS OF OPTICAL COHERENCE
TOMOGRAPHY IMAGES (O.C.T)**

MANDELIAS KONSTANTINOS

PATRA 2012

SUPERVISOR

Assistant Professor *George C. Kagadis*

EXAMINING COMMITTEE

Assistant Professor *George C. Kagadis*

Professor *George Nikiforidis*

Assistant Professor *Dimitrios Karnabatidis*

ACKNOWLEDGEMENTS

I wish to express my gratitude to my supervisor Assistant Professor George C. Kagadis for the assignment of this project and for his guidance throughout this thesis.

I am also grateful to Professor G. Nikiforidis for his faith and confidence towards me and for his contribution in the fulfillment of this thesis.

I would like to thank Dr. S. Tsantis for helping me to acquire knowledge and for his important guidance in wavelet, MRF theory and algorithms. I would also like to thank him for his valuable guidelines in writing scientific articles.

Finally, I wish to express my gratitude to my parents, my brother and my friends for their constant support and encouragement during the years of that work.

Mandelias Konstantinos

Abstract

Purpose: Optical Coherence Tomography (OCT) is a catheter-based imaging method that employs near-infrared light to produce high-resolution cross sectional intravascular images. A new segmentation technique is implemented for automatic lumen area extraction and stent strut detection in intravascular OCT images for the purpose of quantitative analysis of neointimal hyperplasia (NIH). Also a graphical user interface (GUI) is designed based on the employed algorithm.

Methods: Four clinical dataset of frequency-domain OCT scans of the human femoral artery were analysed. First, a segmentation method based on Fuzzy C Means (FCM) clustering and Wavelet Transform (WT) was applied towards inner luminal contour extraction. Subsequently, stent strut positions were detected by utilizing metrics derived from the local maxima of the wavelet transform into the FCM membership function.

Results: The inner lumen contour and the position of stent strut were extracted with very high accuracy. Compared with manual segmentation by an expert physician, the automatic segmentation had an average overlap value of 0.917 ± 0.065 for all OCT images included in the study. Also the proposed method and all automatic segmentation algorithms utilised in this thesis such as k-means, FCM, MRF – ICM and MRF – Metropolis were compared by means of mean distance difference in mm and processing time in sec with the physician's manual assessments.. The strut detection procedure successfully identified 9.57 ± 0.5 struts for each OCT image.

Conclusions: A new fast and robust automatic segmentation technique combining FCM and WT for lumen border extraction and strut detection in intravascular OCT images was designed and implemented. The proposed algorithm may be employed for automated quantitative morphological analysis of in-stent neointimal hyperplasia.

Περίληψη

Σκοπός: Η τομογραφία οπτικής συνοχής (OCT) είναι μια απεικονιστική μέθοδος βασισμένη στον καθητηριασμό και χρησιμοποιεί υπέρυθρο φως για να παράγει ένδο-αγγειακές εικόνες – εγκάρσιας τομής με υψηλή ανάλυση. Σε αυτήν την διατριβή, μια νέα τεχνική τμηματοποίησης υλοποιήθηκε για την αυτόματη εξαγωγή της περιοχής του αυλού καθώς και για την ανίχνευση των «strut» στις ένδο-αγγειακές OCT εικόνες με σκοπό την ποσοτική ανάλυση της υπερπλασίας. Επίσης ένα εύκολο στην χρήση περιβάλλον γραφικών για καθημερινή κλινική χρήση σχεδιάστηκε με τον υλοποιημένο αλγόριθμο.

Μέθοδοι: Τέσσερις OCT κλινικές εξετάσεις πεδίου-συχνότητας της ανθρώπινης μηριαίας αρτηρίας αναλύθηκαν. Η προτεινόμενη μέθοδος τμηματοποίησης για την εξαγωγή του εσωτερικού περιγράμματος αυλού, είναι βασισμένη στον Fuzzy C-Means (FCM) clustering και τον μετασχηματισμό κυματιδίου. Στη συνέχεια, οι θέσεις των «strut» εντοπίστηκαν χρησιμοποιώντας διάφορες τοπικές παραμέτρους που προέρχονται από τα τοπικά μέγιστα του μετασχηματισμού κυματιδίων εντός της FCM συνάρτησης.

Αποτελέσματα: Το εσωτερικό περίγραμμα αυλού και η θέση των «strut» εξήχθηκαν με πολύ μεγάλη ακρίβεια. Σε σύγκριση με την ποσοτική αξιολόγηση από έναν ειδικό ιατρό, η αυτόματη τμηματοποίηση είχε μέση τιμή επικάλυψης $0,917 \pm 0,065$ για όλες τις OCT εικόνες που περιλαμβάνονται στη μελέτη. Επίσης, έγινε σύγκριση με τους k-means, FCM, ICM και Metropolis αυτόματους αλγόριθμους τμηματοποίησης για εξαγωγή του εσωτερικού περιγράμματος αυλού και επέδειξε υψηλής ακρίβειας αποτελέσματα στον μικρότερο δυνατό χρόνο επεξεργασίας. Η διαδικασία ανίχνευσης «strut» προσδιόρισε επιτυχώς $9.57 \pm 0,5$ «strut» για κάθε OCT εικόνα.

Συμπεράσματα: Μια νέα αποτελεσματική και γρήγορη αυτόματη τεχνική τμηματοποίησης που συνδυάζει FCM και WT για την εξαγωγή των ορίων του αυλού και την ανίχνευση των «strut» στις ένδο-αγγειακές εικόνες OCT σχεδιάστηκε και υλοποιήθηκε. Ο προτεινόμενος αλγόριθμος μπορεί να χρησιμοποιηθεί για την αυτοματοποιημένη ποσοτική μορφολογική ανάλυση της υπερπλασίας.

TABLE OF CONTENTS

CHAPTER 1 - Optical Coherence Tomography Physics & Instrumentation	
.....	1
Introduction	1
1.1 Anatomic Considerations	1
1.2 Fundamentals	2
1.3 Principles Of Operation	2
1.4 Equipment	7
1.4.1 Time-Domain Oct	8
1.4.2 Fourier-Domain Oct	8
CHAPTER 2 - Clustering Algorithms	12
Introduction	12
2.1 Basic Clustering Algorithms	13
2.2 K-Means Clustering Algorithm	15
2.3 Fuzzy C-Means Clustering (FCM) Algorithm	17
2.4 Markov Random Field (MRF)	20
2.4.1 ICM Algorithm	22
2.4.2 Simulated Annealing Algorithms	24
2.4.3 Metropolis Algorithm	25
CHAPTER 3 - The Wavelet Transform (WT)	27
3.1 Wavelet Theory	27
3.2 Requirements For The Wavelet	29
3.3 1-D Continuous Wavelet Transform	29
3.4 2-D Continuous Wavelet Transform	30
CHAPTER 4 - Fast And Robust Vessel Lumen Segmentation And Strut	
Detection In Intravascular Oct	32
Introduction	32
4.1 Previous Work	32
4.2 Oct Clinical Dataset	36
4.3 Lumen Wall Delineation	37
4.4 Stent Strut Position Detection	43
4.5 Hyperplasia Estimation	47

4.6 Quantitative Results	50
4.7 Graphical User Interface Implementation	52
4.8 Discussion	54
REFERENCES.....	56

CHAPTER1

OPTICAL COHERENCE TOMOGRAPHY

PHYSICS & INSTRUMENTATION

Introduction

Optical coherence tomography (OCT) is an emerging optical imaging technology that performs high-resolution, cross-sectional tomographic imaging of internal structure in biological systems and materials [1,2]. OCT is analogous to ultrasound B mode imaging except that it uses light instead of sound. Image resolutions of 1–15 μm can be achieved, over one order of magnitude higher than conventional ultrasound. OCT performs imaging by measuring the echo time delay and intensity of backscattered light from internal microstructure in the tissue. Compared to traditional intravascular ultrasound (IVUS), OCT has a ten-fold higher image resolution given the use of light rather than sound. This advantage has seen OCT successfully applied to the assessment of atherosclerotic plaque, stent apposition and tissue coverage, introducing a new era in intravascular coronary imaging. The origins of OCT date back to 1990 and introduced by David Huang [1].

1.1 Anatomic Considerations

Principally, all epicardial coronary arteries, venous or arterial grafts accessible by a guiding catheter, are eligible for OCT imaging. Considerations regarding anatomy and patient characteristics arise from the fact (a) that OCT imaging requires a blood-free environment and (b) from OCT catheter design. As the imaging procedure demands temporary blood removal and flush (e.g. lactated ringers or X-ray contrast medium), it should not be performed in patients with severely impaired left ventricular function or those presenting with hemodynamic compromise. Further, OCT should be used with caution in patients with single remaining vessel or those with markedly impaired renal function. Lesions that are ostially or proximally located cannot be adequately imaged using proximal balloon occlusion and thus, a non-occlusive

technique may be preferred in these circumstances. Large caliber vessels or very tortuous vessels often preclude complete circumferential imaging as a result of a non-central, non-coaxial position of the OCT imaging probe within the vessel. These anatomic limitations seem to be significantly attenuated in Fourier-domain OCT, as the pullback speed is much higher and as a result, the duration of ischemia and the amount of potentially nephrotoxic flush is much lower. Increased penetration depth and scanning range allow imaging of the complete circumference of large and tortuous vessels. The design as short monorail catheter enables to negotiate even complex lesions by selecting an appropriate standard guide wire. As there is no proximal balloon occlusion necessary, also ostial lesions, bifurcations and large vessels can be visualized [2].

1.2 Fundamentals

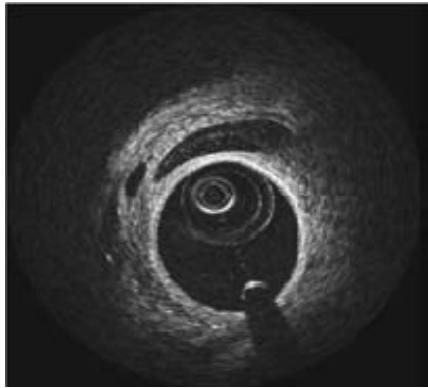
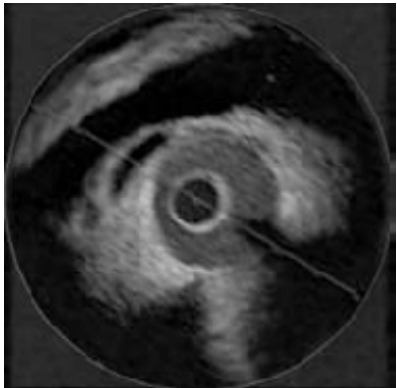
The principle is analogous to pulse-echo ultrasound imaging, however light is used rather than sound to create the image. Whereas ultrasound produces images from backscattered sound “echoes,” OCT uses infrared light waves that reflect off the internal microstructure within the biological tissues. The use of light allows for a 10 fold higher image resolution, however this is at the expense of a reduced penetration depth and the need to create a blood-free environment for imaging. In coronary arteries blood (namely red blood cells) represents a nontransparent tissue causing multiple scattering and substantial signal attenuation. As a consequence, blood must be displaced during OCT imaging. This procedure is potentially causing ischemia in the territory of the artery under study. The need for balloon occlusion and intra-coronary flush are at the forefront of emerging developments to simplify the OCT image acquisition process. Automated catheter pullbacks at very high speed are currently under development in OCT systems using optical Fourier-domain imaging. Faster pullback speeds offer the potential to scan an entire stent within a matter of 5-6 seconds [2].

1.3 Principles Of Operation

OCT utilizes a near infrared light source (approx 1300nm wavelength) in combination with advanced fibre-optics to create a dataset of the coronary artery. Both the

bandwidth of the infrared light used and the wave velocity are orders of magnitude higher than in medical ultrasound. The resulting resolution depends primarily on the ratio of these parameters, and is one order of magnitude larger than that of IVUS: the axial resolution of OCT is about 15 μm . The lateral resolution is mainly determined by the imaging optics in the catheter and is approximately 25 μm . The imaging depth of approximately 1.0-1.5mm within the coronary artery wall is limited by the attenuation of light in the tissue [TABLE 1.1].

Table 1.1: Comparison OCT and IVUS

	OCT	IVUS
		
Axial Resolution	10-20 μm	100-150 μm
Penetration depth	1.5-2 mm	4-8 mm
Probe size	0.4 mm	1.1 mm
Pullback speed	0.5 mm/s	Up to 40 mm/s
Blood removal needed	Yes	No
Plaque characterization	Yes	Yes
Fibrous cap measurement	Yes	No
Vessel remodelling	No	Yes

OCT is analogous to ultrasound imaging but uses light instead of sound. Cross-sectional images are generated by measuring the echo time delay and intensity of light that is reflected or backscattered from internal structures in tissue [1]. Because the velocity of light is extremely high, the echo time delay cannot be measured directly. Instead, it is necessary to use correlation or interferometry techniques. One

method for measuring the echo time delay of light is to use low-coherence interferometry.

Low-coherence interferometry was first developed for measuring reflections in fiber optics and optoelectronic devices [3–5]. The first applications of low-coherence interferometry in biomedicine were in ophthalmology to perform precision measurements of axial eye length and corneal thickness [6, 7]. Low-coherence interferometry measures the echo time delay and intensity of backscattered light by interfering it with light that has traveled a known reference path length and time delay.

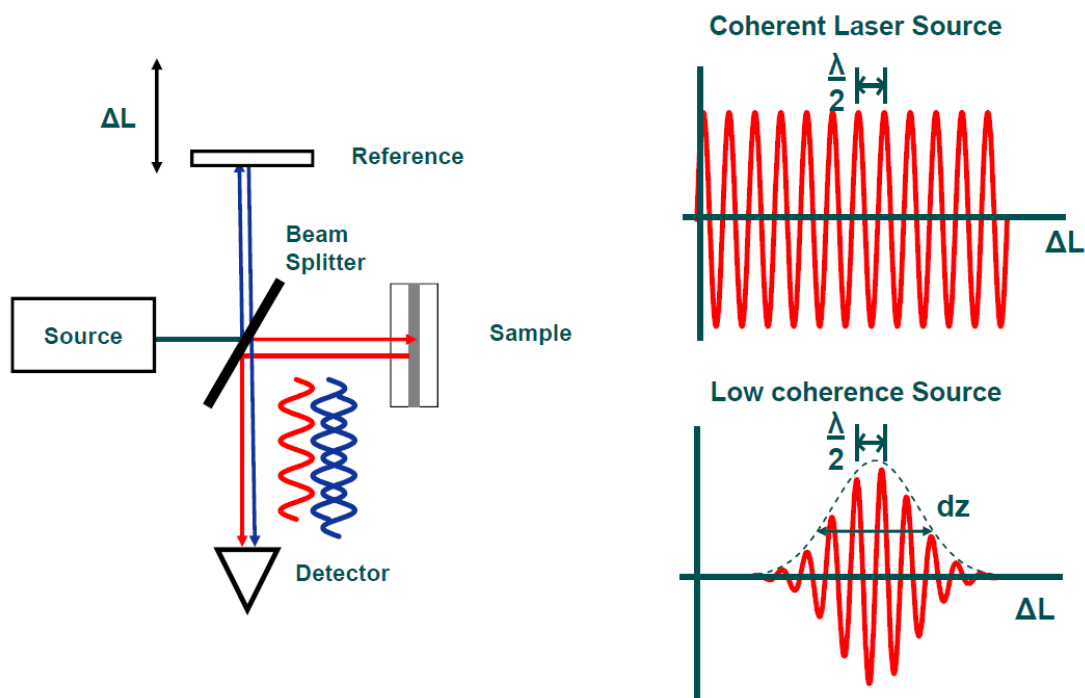


Figure 1.1 OCT measures the echo time delay of reflected light by using low-coherence interferometry. The system is based on a Michelson-type interferometer. Reflections or backscattering from the object being imaged are correlated with light which travels a reference path.

Measurements are performed using a Michelson-type interferometer (*figure 1.1*). Light from a source is directed onto a beam splitter, and one of the beams is incident onto the sample to be imaged, while the second beam travels a reference path with a variable path length. The backscattered light from the sample is interfered with reflected light from the reference arm and detected with a photodetector at the

interferometer output. If the light source is coherent, then interference fringes will be observed as the relative path lengths are varied. However, if low-coherence light or short pulses are used, then interference occurs only when the two path lengths match to within the coherence length of the light. The echo time delay and intensity of backscattered light from sites within the sample can be measured by detecting and demodulating the interference output of the interferometer while scanning the reference path length. This method is analogous to heterodyne optical detection in optical communications.

Figure 1.2 is a schematic illustrating how OCT performs cross-sectional imaging. The optical beam is focused into the sample being imaged, and the echo time delay and intensity of the backscattered light are measured to yield an axial backscattering profile. The incident beam is then scanned in the transverse direction, and the axial backscattering profile is measured at several transverse positions to yield a two-dimensional data set. This data set represents the optical backscattering through a cross section of the tissue. The data is displayed as a logarithmic gray scale or false color image.

One of the advantages of OCT is that it can be implemented using compact fiber optic components and integrated with a wide range of medical instruments. Figure 1.3 shows a schematic of an OCT system using fiber optic Michelson-type interferometer. A low-coherence light source is coupled into the interferometer, and the interference at the output is detected with a photodiode. One arm of the interferometer emits a beam that is directed and scanned on the sample that is being imaged, while the other arm of the interferometer is a reference arm with a scanning delay line. The system can be interfaced to microscopes, hand held imaging probes, as well as catheters and endoscopes.

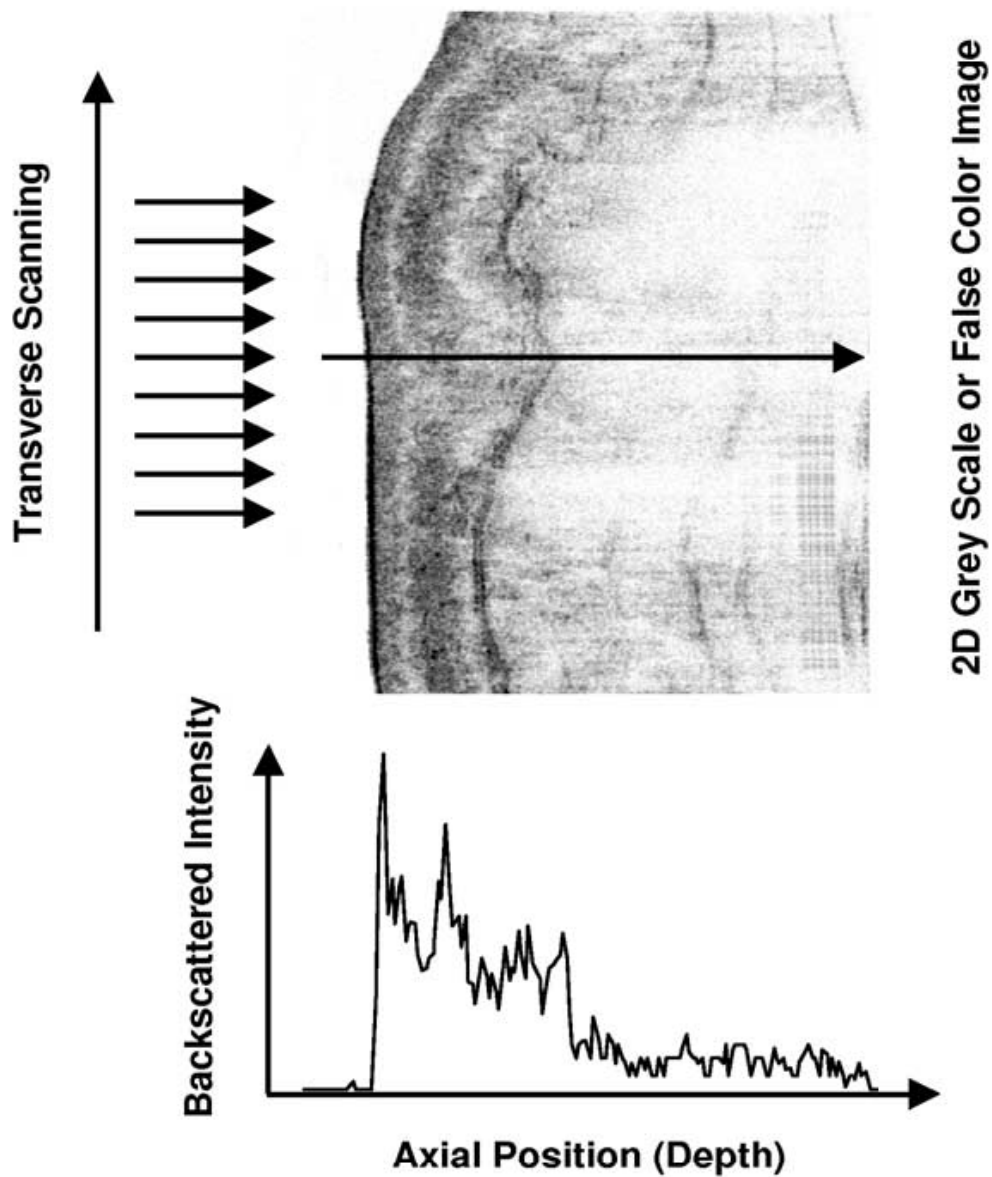


Figure 1.2 Cross-sectional images are constructed by performing measurements of the echo time delay of light at different transverse positions. The result is a two-dimensional data set that represents the backscattering in a cross-sectional plane of the tissue.

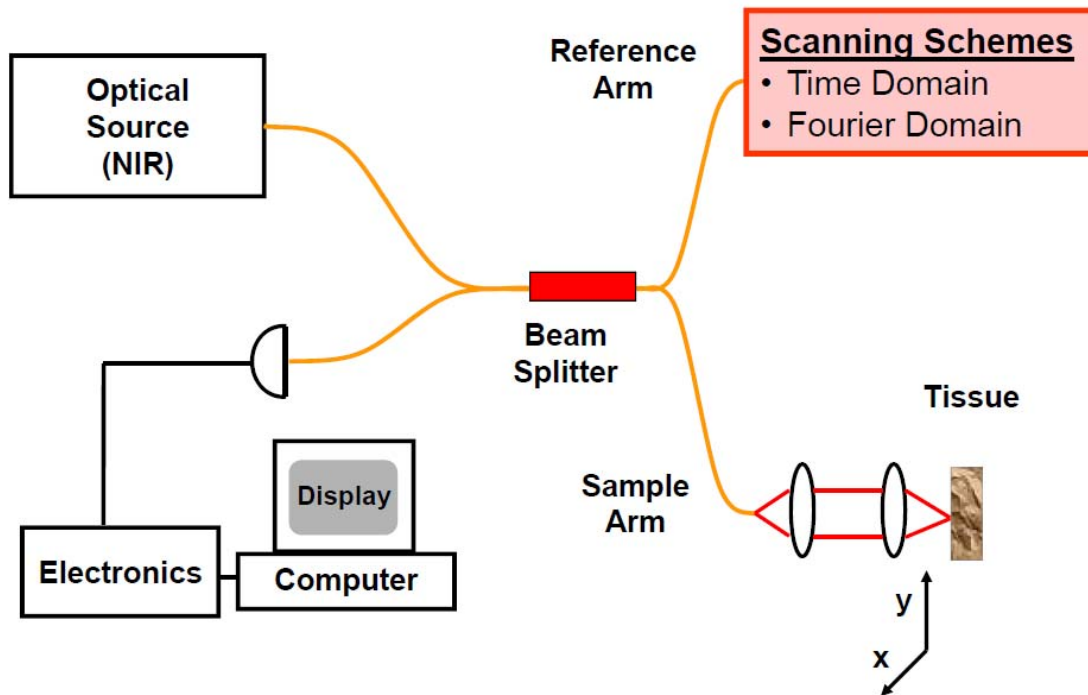


Figure 1.3 Schematic of OCT instrument based on a fiber-optic implementation of a Michelson interferometer. One arm of the interferometer is interfaced to the measurement instrument and the other arm has a scanning delay line. The system shown is configured for high-speed catheter/endoscope based imaging.

1.4 Equipment

The equipment for intracoronary OCT generally consists in an OCT imaging catheter, a motorized pullback device and an imaging console, that contains the light source, signal processing units, data storage and display [8]. The imaging catheter is part of the sample arm of the interferometer. The optical signal is transmitted by a single-mode fiber, which is fitted with an integrated lens micro-prism assembly to focus the beam and direct it towards the tissue. The focus is approximately 1mm outside the catheter. In order to scan the vessel lengthwise, the catheter-imaging tip is pulled back while rotating, usually inside a transparent sheath, allowing to collect a three dimensional dataset of the coronary artery. Both rotary and pullback motion are driven proximally by a motor outside the patient.

1.4.1 Time-Domain Oct

In time-domain (TD-) OCT, the length of the reference arm is scanned over a distance of typically a few millimetres, by moving a mirror. The point from which intensity is collected from the sample arm is moved through the tissue accordingly, and the amplitude of the recorded interferogram in a scan corresponds to the reflectivity of the tissue along the direction of the sample beam. By scanning the beam along the tissue, in a rotary fashion for intravascular imaging, an image is built up out of neighbouring lines. Figure 1.4 shows the currently commercially available TD-OCT system (Lightlab Imaging, Westford, MA, USA).

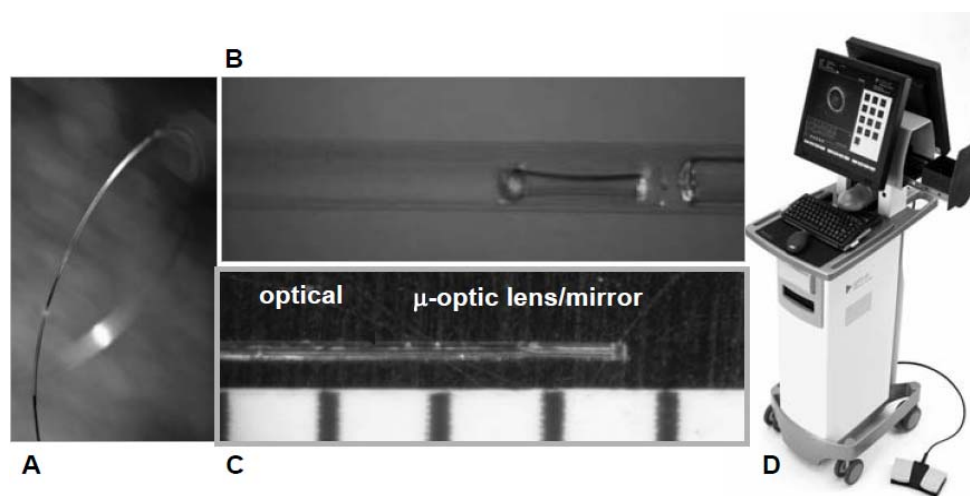


Figure 1.4 The currently commercially available TD-OCT system (Lightlab Imaging, Westford, MA, USA). A) The OCT imaging wire with an outer diameter of 0.019 inch B) Magnification of the distal catheter tip C) Magnification of the 0.006 inch rotating single-mode fibre-optic core, located within the distal sleeve of the imaging wire D) Imaging console with pullback device allowing for real-time image display and data storage.

1.4.2 Fourier-Domain Oct

A new generation of OCT systems operates in the frequency (rather than time-) domain, also called Fourier domain. The interferogram is detected as a function of wavelength, either by using a broadband source as in the time domain systems, and spectrally resolved detection, or alternatively by incorporating a novel wavelength-swept laser source [9] [10][TABLE 1.2]. This latter technique is also called “swept-

source OCT”, or optical frequency domain imaging (OFDI), and capitalizes most effectively on the higher sensitivity and signal-to-noise ratio offered by Fourier domain detection. This development has led to faster image acquisition speeds, with greater penetration depth, without loss of vital detail or resolution, and represents a great advancement on current conventional OCT systems. From the signal received in one wavelength sweep, the depth profile can be constructed by the Fourier transform operation that is performed electronically in the data processing unit. All other components of a Fourier-domain system (the interferometer, the catheter, including the imaging optics, display) are comparable in principle to those in a time-domain OCT system.

Table1.2: Characteristics of time domain OCT (TD-OCT) and Fourier domain OCT (FD-OCT). Characteristics of TD–OCT are given for the commercially available Lightlab Imaging (Westford, MA, USA) system, characteristics of FD–OCT are based on non/commercially available prototypes.

	TD-OCT fixed light source and variable reference mirror	FD-OCT light source with variable wavelength and fixed reference mirror
Axial Resolution	10-20 μm	Up to 7 μm
Penetration depth	1.5-2 mm	1.5-2 mm
Optical core	Image Wire	Integrated in catheter
Maximum pullback speed	3 mm/s	Up to 40 mm/s
Scan diameter	7 mm	>10 mm
Blood removal needed	Yes	Yes

The scan speed, or line rate, in a time-domain-OCT system are limited by the achievable mechanical scan speed of the reference arm mirror, and by the sensitivity of the signal detection [11]. The source wavelength in Fourier-domain OCT can be swept at a much higher rate than the position scan of the reference arm mirror in a time-domain OCT system. In addition, Fourier-domain OCT has a higher sensitivity than time-domain OCT at large line rates and scan depths [12-14]. These features can be put to good use in larger scan speeds, of the order of 105 lines per second. In

a Fourier domain OCT system, the wavelength range of the sweep determines the resolution of the image, while the imaging depth is inversely related to the instantaneous spectral width of the source.

The increased sensitivity of Fourier-domain OCT also allows for larger imaging depths. The attenuation of light by the tissue is the same for time-domain and for Fourier-domain OCT, but the lower noise of the latter makes it possible to discern weaker signals that would be indistinguishable from the background in time-domain OCT. The depth range from which useful anatomical information can be extracted is extended by a factor of about 3 [15]. Clinically, this advantage enables the assessment of coronary micro-structures well beyond the arterial-lumen border.

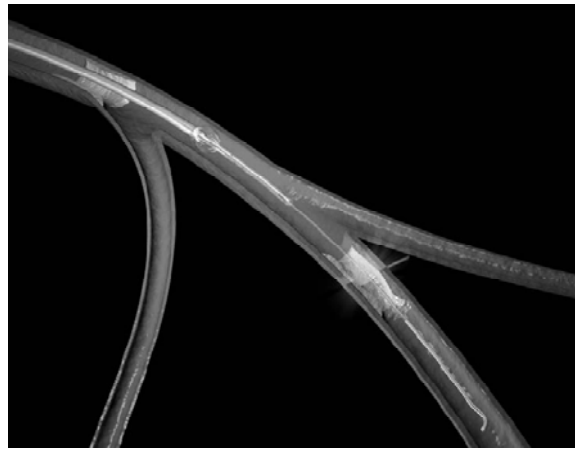


Figure 1.5 Occlusive image acquisition technique (TD OCT imaging Lightlab Imaging, Westford, MA, USA).

Fourier domain OCT systems produce images much faster than standard video-rate, so recorded data has to be replayed for inspection by the operator. Currently, OCT systems scan 200-500 angles per revolution (frame), and 5-10 images per mm in a pullback. If these parameters are maintained with high speed systems, 20 mm/s (or higher) pullback speeds are possible at the same sampling density as conventional OCT data. Figure 1.6 shows different FD-OCT prototypes as used at the Thoraxcenter in 2008.

The high scan speeds have been employed for real-time volumetric imaging of dynamic phenomena including fast pullbacks for intra-coronary imaging with minimal ischemia, [15] and retinal scans with minimal motion artifacts [16]. Imaging

of dynamic phenomena in time, or rather removing motion artifacts, are the prime applications of high-speed OCT. 3-Dimensional rendering of volumes becomes possible if motion during the scan is limited. The high data rate of novel OCT technologies could also be used to increase sampling density, either in the longitudinal (pullback) or angular direction. A smaller spacing between frames in a pullback would lead to a better sampling of small scale features in the arterial or stent geometry that would be missed at 100 μm inter-frame distance. Denser sampling in the angular direction would facilitate speckle filtering in OCT images. Speckle is a major obstacle for the development of parametric and quantitative imaging techniques. These possibilities are still largely unexplored.

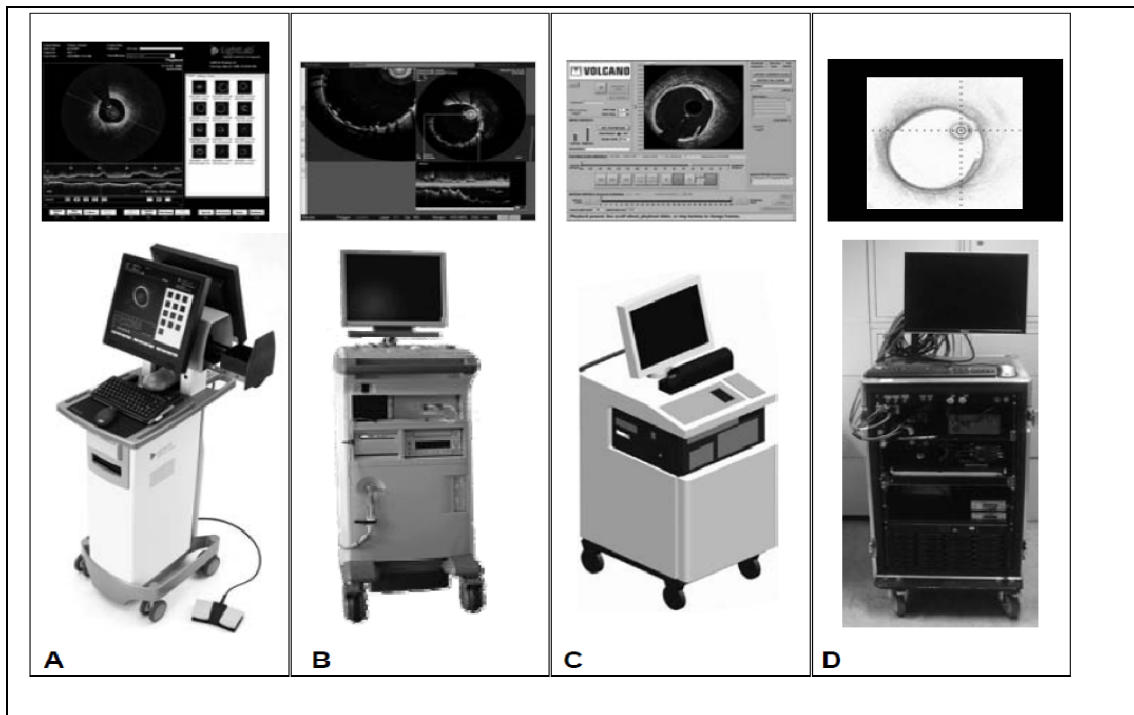


Figure 1.6 Different FD-OCT prototypes as used at the Thoraxcenter in 2008 A) M4 system, Lightlab Imaging, Westford, MA, USA , B) Terumo OCT C) Volcano OCT D) MGH OFDI system (G. Tearney and B. Bouma, Wellman Center for Photomedicine, MGH, Boston, MA, USA).

CHAPTER 2

CLUSTERING ALGORITHMS

Introduction

Clustering is an unsupervised learning task that aims at decomposing a given set of objects into subgroups or clusters based on similarity. The goal is to divide the data-set in such a way that objects (or example cases) belonging to the same cluster are as similar as possible, whereas objects belonging to different clusters are as dissimilar as possible. The motivation for finding and building classes in this way can be manifold [17]. Cluster analysis is primarily a tool for discovering previously hidden structure in a set of unordered objects. In this case one assumes that a 'true' or natural grouping exists in the data. However, the assignment of objects to the classes and the description of these classes are unknown. By arranging similar objects into clusters one tries to reconstruct the unknown structure in the hope that every cluster found represents an actual type or category of objects. Clustering methods can also be used for data reduction purposes. Then it is merely aiming at a simplified representation of the set of objects which allows for dealing with a manageable number of homogeneous groups instead of with a vast number of single objects. Only some mathematical criteria can decide on the composition of clusters when classifying data-sets automatically. Therefore clustering methods are endowed with distance functions that measure the dissimilarity of presented example cases, which is equivalent to measuring their similarity. As a result one yields a partition of the data-set into clusters regarding the chosen dissimilarity relation.

All clustering methods that we consider in this chapter are partitioning algorithms. Given a positive integer K , they aim at finding the best partition of the data into K groups based on the given dissimilarity measure and they regard the space of possible partitions into K subsets only.

A common concept of all described clustering approaches is that they are prototype-based, i.e., the clusters are represented by cluster prototypes M_j , $j=1, \dots, K$. Prototypes are used to capture the structure (distribution) of the data in each cluster. With this representation of the clusters we formally denote the set of prototypes $M = \{M_1, \dots, M_K\}$. Each prototype M_j is an n -tuple of parameters that consists of a cluster center μ_i (location parameter) and maybe some additional parameters about the size and the shape of the cluster. The cluster center μ_i is an instantiation of the attributes used to describe the domain, just as the data points in the data-set to divide. The size and shape parameters of a prototype determine the extension of the cluster in different directions of the underlying domain. The prototypes are constructed by the clustering algorithms and serve as prototypical representations of the data points in each cluster.

2.1 Basic Clustering Algorithms

Clustering algorithms are used extensively not only to organize and categorize data, but are also useful for data compression and model construction [18].

In this section, we present the fuzzy C-means, deriving it from the hard c-means clustering algorithm. The latter one is better known as k-means, but here we call it (hard) C-means to unify the notation and to emphasize that it served as a starting point for the fuzzy extensions. We further restrict ourselves to the simplest form of cluster prototypes at first. That is, each prototype only consists of the center vectors, $C_i = (c_i)$, such that the data points assigned to a cluster are represented by a prototypical point in the data space. We consider as a distance measure d an inner product norm induced distance as for instance the Euclidean distance.

All algorithms described in this section are based on objective functions Q , which are mathematical criteria that quantify the goodness of cluster models that comprise prototypes and data partition. Objective functions serve as cost functions that have to be minimized to obtain optimal cluster solutions. Thus, for each of the following cluster models the respective objective function expresses desired properties of what should be regarded as “best” results of the cluster algorithm. Having defined such a criterion of optimality, the clustering task can be formulated as a function

optimization problem. That is, the algorithms determine the best decomposition of a data-set into a predefined number of clusters by minimizing their objective function. The steps of the algorithms follow from the optimization scheme that they apply to approach the optimum of Q . Thus, in our presentation of the hard and fuzzy c-means we discuss their respective objective functions first. Then we shed light on their specific minimization scheme.

The idea of defining an objective function and have its minimization drive the clustering process is quite universal. Aside from the basic algorithms many extensions and modifications have been proposed that aim at improvements of the clustering results with respect to particular problems (e.g., noise, outliers). Consequently, other objective functions have been tailored for these specific applications. However, regardless of the specific objective function that an algorithm is based on, the objective function is a goodness measure. Thus it can be used to compare several clustering models of a data-set that have been obtained by the same algorithm (holding the number of clusters, i.e., the value of μ).

In their basic forms the hard and fuzzy C-means algorithms look for a predefined number of K clusters in a given data-set, where each of the clusters is represented by its center vector. However, hard and fuzzy C-means differ in the way they assign data to clusters, i.e., what type of data partitions they form. In classical (hard) cluster analysis each datum is assigned to exactly one cluster. Consequently, the hard C-means yield exhaustive partitions of the example set into non-empty and pairwise disjoint subsets. Such hard (crisp) assignment of data to clusters can be inadequate in the presence of data points that are almost equally distant from two or more clusters. Such special data points can represent hybrid-type or mixture objects, which are (more or less) equally similar to two or more types. A crisp partition arbitrarily forces the full assignment of such data points to one of the clusters, although they should (almost) equally belong to all of them. For this purpose the fuzzy clustering approaches presented in Section 2.3 fulfill the requirement that data points have to be assigned to one (and only one) cluster. Data points can belong to more than one cluster and even with different degrees of membership to the different clusters. These gradual cluster assignments can reflect present cluster

structure in a more natural way, especially when clusters overlap. Then the memberships of data points at the overlapping boundaries can express the ambiguity of the cluster assignment.

The shift from hard to gradual assignment of data to clusters for the purpose of more expressive data partitions founded the field of fuzzy cluster analysis. We start our presentation with the hard C-means.

2.2 K-Means Clustering Algorithm

One of the simplest unsupervised clustering techniques is k-means clustering [19, 20]. The procedure follows a simple and easy way to classify a given data set through a certain number of clusters. In this method, from a set of patterns, K number of patterns are randomly chosen as initial cluster centers of the K clusters. In each iteration the patterns are assigned to the cluster having the nearest center; and the centers of the clusters are updated after assignment of all patterns. The center of a cluster is the arithmetic mean of the patterns assigned to it at the previous iteration. Thus if $M = [\mu_1, \mu_2, \dots, \mu_K]$, includes K number of vectors μ_j ($\mu_j, 1 \leq j \leq K$) of cluster prototypes, then after the first iteration μ_1 becomes the arithmetic mean of the patterns assigned to the first cluster at this iteration, μ_2 the arithmetic mean of the patterns assigned to second cluster and so on. It means that the different components of the vector μ_j are the arithmetic means of corresponding component values of the patterns belonging to the jth cluster. This process stops when the centers become fixed i.e. no changes occur from the partitioning point of view.

This process is “partitive” because at every iteration the partitions or boundaries between the clusters are changed and some patterns from one cluster are moved to some other clusters. The boundaries are crisp or hard as each pattern is assigned to only one cluster.

The k-means algorithm basically minimizes the following objective function

$$Q = \sum_{j=1}^K \sum_{i=1}^n \|v_i^j - \mu_j\|^2 \quad (2.1)$$

where v_i^j the i th sample of j th class K_j and μ_j the center of the j th cluster defined as the mean of $v_i \in K_j$. Also $\|v_i^j - \mu_j\|^2$ (Euclidean distance).

Distance equations that we can use are:

Euclidean
$$d(x, y) = \sqrt{\sum_{i=1}^n (x_i - y_i)^2}$$

Hamming
$$d(x, y) = \sum_{i=1}^n |x_i - y_i|$$

Tchebyshev
$$d(x, y) = \max |x_i - y_i|, i = 1, 2, \dots, n$$

Minkowski
$$d(x, y) = \sqrt[p]{\sum_{i=1}^n (x_i - y_i)^p}, p > 0$$

Camberra
$$d(x, y) = \sum_{i=1}^n \frac{|x_i - y_i|}{x_i + y_i}, x_i \text{ and } y_i > 0$$

The K-means algorithm is composed of the following steps:

1. Initialize the number of classes K and centroids v_j .
2. Assign each pixel or voxel to the group whose centroid is the closest.
3. After all pixels have been assigned, recalculate the centroids.
4. Repeat steps 2 and 3 until the centroids no longer change.

The k-means algorithm does not necessarily find the most optimal configuration, corresponding to the global objective function minimum. The algorithm is also significantly sensitive to the initial randomly selected cluster centres. The k-means algorithm can be run multiple times to reduce this effect. K-means is a simple algorithm that has been adapted to many problem domains.

2.3 Fuzzy C-Means Clustering (Fcm) Algorithm

Fuzzy cluster analysis allows gradual memberships of data points to clusters measured as degrees in $[0,1]$. This gives the flexibility to express that data points can belong to more than one cluster. This method was developed by Dunn in 1973 [21] and improved by Bezdek in 1981 [22]. Furthermore, these membership degrees offer a much finer degree of detail of the data model. Aside from assigning a data point to clusters in shares, membership degrees can also express how ambiguously or definitely a data point should belong to a cluster. The concept of these membership degrees is substantiated by the definition and interpretation of fuzzy sets (Zadeh, 1965) [23].

Let $V = \{v_1, \dots, v_n\}$ be the set of given examples and let c be the number of clusters $1 < c < n$. Then we call u_{ij} a probabilistic cluster partition of V if

$$\sum_{j=1}^n u_{ij} > 0, \forall i = \{1, \dots, C\} \quad (2.2)$$

and

$$\sum_{i=1}^c u_{ij} = 1, \forall j = \{1, \dots, n\} \quad (2.3)$$

The $u_{ij} \in [0,1]$ are interpreted as the membership degree of datum v_j to cluster i relative to all other clusters. Constraint (2.2) guarantees that no cluster is empty. This corresponds to the requirement in classical cluster analysis that no cluster, represented as (classical) subset of V , is empty. Condition (2.3) ensures that the sum of the membership degrees for each datum equals 1. This means that each datum receives the same weight in comparison to all other data and, therefore, that all data are (equally) included into the cluster partition. As a consequence of both constraints no cluster can contain the full membership of all data points. Furthermore, condition (2.3) corresponds to a normalization of the memberships per datum. Thus the membership degrees for a given datum formally resemble the probabilities of its being a member of the corresponding cluster.

After defining probabilistic partitions we can turn to developing an objective function for the fuzzy clustering task. Certainly, the closer a data point lies to the center of a cluster, the higher its degree of membership should be to this cluster. Following this rationale, one can say that the distances between the cluster centers and the data points (strongly) assigned to it should be minimal. Hence the problem to divide a given data-set into c clusters can (again) be stated as the task to minimize the squared distances of the data points to their cluster centers, since, of course, we want to maximize the degrees of membership. The probabilistic fuzzy objective function Q is thus based on the least sum of squared distances.

More formally, a fuzzy cluster model of a given data-set V into c clusters is defined to be optimal when it minimizes the objective function:

$$Q_{fcm} = \sum_{j=1}^n \sum_{i=1}^C u_{ij}^m \|v_j - \mu_i\|^2 \quad 1 \leq m < \infty \quad (2.4)$$

under the constraints (2.2) and (2.3) that have to be satisfied for probabilistic membership degrees in Q . The condition (2.3) avoids the trivial solution of minimization problem, i.e., $u_{ij}=0 \forall i, j$. The normalization constraint (2.3) leads to a 'distribution' of the weight of each data point over the different clusters. Since all data points have the same fixed amount of membership to share between clusters, the normalization condition implements the known partitioning property of any probabilistic fuzzy clustering algorithm. The parameter m , $m > 1$, is called the fuzzifier or weighting exponent. The actual value of m determines the 'fuzziness' of the classification. The generalization for exponents $m > 1$ that lead to fuzzy memberships has been proposed in Bezdek, 1973 [25]. With higher values for m the boundaries between clusters become softer, with lower values they get harder. Usually $m=2$ is chosen.

The membership degrees have to be chosen according to the following formula that is independent of the chosen distance measure [22, 24] :

$$u_{ij}^m = \frac{1}{\sum_{k=1}^c \left(\frac{\|v_j - \mu_i\|}{\|v_j - \mu_k\|} \right)^{\frac{2}{m-1}}} \quad (2.5)$$

In this case there exists a cluster i with zero distance to a datum v_j , $u_{ij}=1$ and $u_{kj}=0$ for all other clusters $k \neq i$. The above equation clearly shows the relative character of the probabilistic membership degree. It depends not only on the distance of the datum v_j to cluster i , but also on the distances between this data point and other clusters.

The cluster center estimated:

$$\mu_i = \frac{\sum_{j=1}^n u_{ij}^m v_j}{\sum_{j=1}^n u_{ij}^m} \quad (2.6)$$

The fuzzy c-means algorithm is composed of the following steps:

1. Choose the number of clusters or region.
2. Assign pixels their initial membership values according to equation (2.3).
3. Compute the centroid for each cluster, and the membership values using the formula in Equations (2.5, 2.6).
4. Iterate until $\max \|u_{ij}^{k+1} - u_{ij}^k\| < \varepsilon$ where k is the iteration number and ε is the error threshold; otherwise return to step 2.
5. Assign each pixel the cluster number for which its membership is maximum.

Where:

c - the number of cluster centers or data subsets

m - the weighting exponents

$\|v_j - \mu_i\|^2$ - the distance measure between object v_j and cluster center μ_i ;

n - the total number of pixels in image;

u_{ij} - the fuzzy membership membership matrix

μ_i - the cluster center for subset i in feature space;

U – the fuzzy c -partition

Q - objective function

2.4 Markov Random Field (MRF)

Markov random field (MRF) theory provides a convenient and consistent way of modeling context dependent entities such as image pixels and other spatially correlated features. This is achieved through characterizing mutual influences among such entities using MRF probabilities. The practical use of MRF models is largely ascribed to the equivalence between MRFs and Gibbs distributions established by Hamersley and Clifford (1971) [26] and further developed by Besag (1974) [27] for the joint distribution of MRFs. This enables us to model vision problems by a *mathematically* sound yet tractable means for the image analysis in the Bayesian framework Grenander 1983 [28], Geman and Geman 1984 [29]. From the *computational* perspective, the local property of MRFs leads to algorithms which can be implemented in a local and massively parallel manner. Furthermore, MRF theory provides a foundation for multi-resolution computation Gidas 1989 [30].

For the above reasons, MRFs have been widely employed to solve vision problems at all levels. Most of the MRF models are for low level processing. These include image restoration and segmentation, surface reconstruction, edge detection, texture analysis, optical flow, shape from X , active contours, deformable templates, data fusion, visual integration, and perceptual organization. The use of MRFs in high level vision, such as for object matching and recognition, has also emerged in recent years.

MRF modeling combines conditional (local intensity distribution) with contextual (intensity similarity within small neighborhoods) information under the Bayesian framework in order to estimate the true intensities of the image rather than those based only on the conditional information [27]. It assumes that the class probability of a pixel is only dependent on class membership of its spatial neighbors (also called

lattice) which in turn reduces the possible influence of noise and overlapping structures. The model assumption that the conditional distribution depends on the pixels in the near neighborhood is subject to the Bayesian framework which states that the decision rule for labeling an image pixel combines the conditional intensity distribution of an individual region with prior knowledge regarding that region [31, 29].

Given the fact that the observed image y is a realization of a random field Y , x^* is the true unknown label of the observed pixel, and \hat{x} indicates the estimate of x^* , the main objective of the MRF segmentation model is to find \hat{x} given the observed image y .

Let's assume that $P(X)$ is our prior knowledge and $P(Y|X)$ is the probability of realizing the observed image given the regions distribution in the image. $P(Y|X - \text{Conditional Intensity Distribution})$

Then, in accordance to Bayes theorem

$$P(X|Y) = \frac{P(Y|X)P(X)}{P(Y)} \quad (2.7)$$

where, $P(X|Y)$ is our posterior probability. The most widely used conditional intensity distribution is the Gaussian distribution, whose function, given the class x_s is given by:

$$P(Y = y | X = x_s) = \frac{1}{\sqrt{2\pi\sigma_s^2}} \exp\left(-\frac{(y - \mu_s)^2}{\sigma_s^2}\right) \quad (2.8)$$

Where, μ_s and σ_s are the distribution parameters of class x_s . μ_s and σ_s are the mean value and the standard deviation.

$P(X - \text{Contextual information})$ estimated by:

$$P(X = x) = \exp\{-\beta U(x)\} \quad (2.9)$$

Then, \hat{x} can be obtained by taking the posterior's probability natural logarithm and minimizing its negative resultant:[27] (minimizing its negative resultant is faster from maximizing so for this reason it is used).

$$\hat{x} = \arg \min_x (-\log(P(X | Y))) = \quad (2.10)$$

$$\arg \min (-\log p(y | x) - \log p(x)) = \quad (2.11)$$

Substituting equations 2.8 and 2.9 in equation 2.7, the final assessment of \hat{x} obtained through the calculation of the Minimum a Posteriori (MAP) in the following equation:

$$\hat{x} = \arg \min_{x_s \in L} \left\{ \frac{y - \mu_s}{\sigma_s} + \frac{1}{2} \log(2\pi\sigma_s^2) + \beta U(x_s) \right\} \quad (2.12)$$

Where, $U(x_s)$ is the number of pixels in the neighborhood that have color x_s . and β is a positive constant that controls the interaction between the pixels within the neighborhood.

A number of approaches has been proposed to solve this difficult optimization problem. The solutions can, in general, be viewed under two categories: deterministic or stochastic. In the following sections, we will discuss Besag's deterministic approach known as the iterated conditional modes (ICM algorithm) and the stochastic approach, Metropolis algorithm.

2.4.1 Icm Algorithm

The iterated conditional modes (ICM) algorithm, which is an approximate solution to the MAP estimate, was proposed by Besag [27]. The ICM solves the minimization problem by sequentially updating (i.e., raster scanning the image) labels by minimizing the following equation at each pixel s:

$$\hat{x} = \arg \min_{x_s \in L} \left\{ \frac{y - \mu_s}{\sigma_s} + \frac{1}{2} \log(2\pi\sigma_s^2) + \beta U(x_s) \right\} \quad (2.12)$$

we will refer to the expression inside the brackets as total energy, which is the sum of the negative log-likelihood and the Gibbs energy. β is a positive constant that controls the size of clustering or interaction between the sites.

The energy function $U(x)$, which we will also be referring to as Gibbs energy, has the

following form:

$$U(x) = \sum_{c \in C} V_c(x_c) \quad (2.13)$$

where C denotes the set of cliques* for N_s (N_s denote the neighborhood of s). Note that the sum runs over all clique configurations. V_c is the potential function associated with a clique. It is a function that maps a clique configuration to a real number, that is, $V_c: I \rightarrow R$. The potential function is applicable to all the neighborhoods over the image space. A widely used two point clique potential can be given by:

$$V_c(x) = \begin{cases} -1 & x_s = x_r, s, r \in C \\ 1 & x_s \neq x_r, s, r \in C \end{cases} \quad (2.14)$$

In this formulation, the potential function will be equal to -1 the pair have the same intensities and +1 otherwise.

$(i-1, j-1)$	$(i-1, j)$	$(i-1, j+1)$
$(i, j-1)$	(i, j)	$(i, j+1)$
$(i+1, j-1)$	$(i+1, j)$	$(i+1, j+1)$

*A clique is a subset of points $c \in C$, which are all neighbors of each other.

Let's see how ICM algorithm works:

1. The picture is subject to an initial clustering either automatically or manually.
2. For each Pixel and depending on the number of final clusters the sum of the two Energies estimated ($E_{\text{total}} = \text{log-likelihood} + \text{Gibbs Energy}$) (Energies $E_{\text{total}(x1)}$ and $E_{\text{total}(x2)}$ for labels(1 & 2).
3. For the final price of the Pixel \hat{x} select the one (label) which has the lowest energy.

4. This process is repeated in the entire pixels of the image. As a stopping condition we have a predetermined number of repetitions or a threshold obtained (for example, the energy change is less than a certain threshold).

The performance of the ICM algorithm depends heavily on the initial labeling. If a good initial labeling is possible, the ICM algorithm can quickly converge to a desired solution. If a reasonably good initial labeling is not possible, the stochastic algorithm, which will be discussed in the following sections, may be a better choice. Of course, if they can be executed in a reasonable time. For initial clustering can be used basic clustering algorithms, as k-means etc.

2.4.2 Simulated Annealing Algorithms

In this section, we will discuss a simulated annealing-(SA)-based algorithm that solve the MAP estimate in a manner similar to the physical annealing process that occurs in matters. The first simulated annealing algorithm was proposed by Metropolis et al. in 1953 [32]. It was motivated by simulating the physical process of annealing solids. In a physical annealing process, the matter is heated at a very high temperature and then gradually and very slowly cooled to reach the ground state. Inspired by the physical annealing, the SA-based solutions introduce a temperature variable, similar to the physical temperature in concept, into our energy functions. This variable will allow us to start our optimization process from a state in which all the configurations have equal probability, in other words, from a very hot state. Then, by gradually decreasing the temperature variable, we will be reaching to the global solution. Simulated annealing is a local search algorithm capable of escaping from local optima. The principal advantage of these approaches is that the performance of the optimization is no longer dependent on initial labeling. Kirkpatrick et al. were the first to introduce simulated annealing to optimization problems in 1982 [33]. Since then, simulated annealing has been widely used in combinatorial optimization problems and has achieved good results on a variety of problem instances.

We use E_n and E_c represent the new energy and current energy respectively. E_n is always accepted if it satisfies $E_n < E_c$, but if $E_n \geq E_c$ the new energy level is only

accepted with a probability as specified by $\exp(-(\Delta E)/T)$, where T is the current temperature. Hence, worse solutions are accepted based on the change in solution quality which allows the search to avoid becoming trapped at local minima. The temperature is then decreased gradually and the annealing process is repeated until no more improvement is reached or any termination criteria have been met.

2.4.3 Metropolis Algorithm

The method of Metropolis begins by choosing randomly a new value x' with uniform probability. If the energy is lowered by the replacement of x with x' , the variable is set to this new value. If the energy is increased, then a random number u with uniform distribution between 0 and 1 is generated, and the variable is changed by x' only if $\Delta E/T_k$ is greater than u . Otherwise the variable retains its previous value x .

Note that the previous algorithm is in fact trying to minimize:

$$(\log \sigma_s + (y_s - \mu_s) / \sigma_s + \beta U(x_s)) / T \quad (2.15)$$

where T is the temperature parameter. Similar to the physical annealing process, we need to start with a high temperature and cool it down by decreasing the temperature very slowly. The most commonly used cooling schedule is $T_{k+1} = C \cdot T_k$, where C takes on values in the range $[0.97, 1)$. A value of 0.97 seems to give acceptable results. We will use $T_k = 4$ as the initial temperature. Note that this temperature has no physical relevance in terms of absolute value.

To understand better how the algorithm works we present the pseudo code for 2-D images with two regions.

PSEUDO CODE

Function Metropolis **returns** the segmented image

Inputs: The labeled image with two regions with labels x_i where $i = 1, 2$

K = number of iterations.

The original image

Select an initial temperature T_k

for $k = 1:K$ Let k be the iteration index and set $k=1$

Draw a random uniform number u in the range $(0,1)$

for $s = 1:N$ Let s be the site of the pixel in the original image and N the cluster.

Go to pixel s

Calculate the total energies $E(x_1)$ and $E(x_2)$ for labels x_1 and x_2

Calculate $\Delta E = E(x_2) - E(x_1)$

if $\Delta E/T_k < 0$

Assign the label x_2 to the pixel s

else if $\Delta E/T_k > u$

Assign the label x_2 to the pixel s

else

do not change the label

$k \leftarrow k + 1$ and $T_{k+1} \leftarrow C \cdot T_k$ $C =$ a standard constant.

CHAPTER 3

THE WAVELET TRANSFORM

3.1 Wavelet Theory

Wavelets are an extension of windowed Fourier analysis by Gabor [34], in which through a fixed window a large number of oscillations are used for detecting high frequencies, whereas a small number is used to detect low frequencies. However, in the first case the window is 'blind' to smooth events and in the second case the window probably will miss a brief change. Instead of a fixed window and a variable number of oscillations Morlet and Grossman [35] employed a 'mother wavelet' which is stretched or compressed to change the size of the window, thus providing a decomposition of the signal at different scales (frequency bands) (figure3.1a) and it can be moved to various locations on the signal (figure3.1b). Wavelets are used to transform the signal under investigation into another representation which presents the signal information in a more useful form. This transformation of the signal is known as the wavelet transform. Mathematically speaking, the wavelet transform is a convolution of the wavelet function with the signal.

The wavelets size variation due to dilation permits them to automatically adapt to the different components of the signal. A small window (high frequency band) detects rapid high-frequency components and a large window (low frequency band) traces slow low-frequency components. The wavelet transform gives a representation that has good localization in both frequency and space [36-38]. The localization in frequency implies a correspondence between a scale of the wavelet transform and a frequency band. The overall study across all available frequency bands is called multi-resolution analysis [39-41]. The wavelet transform is divided in two main categories: the continuous wavelet transform (CWT) and the discrete wavelet transform (DWT) which we will not concern and we will not describe.

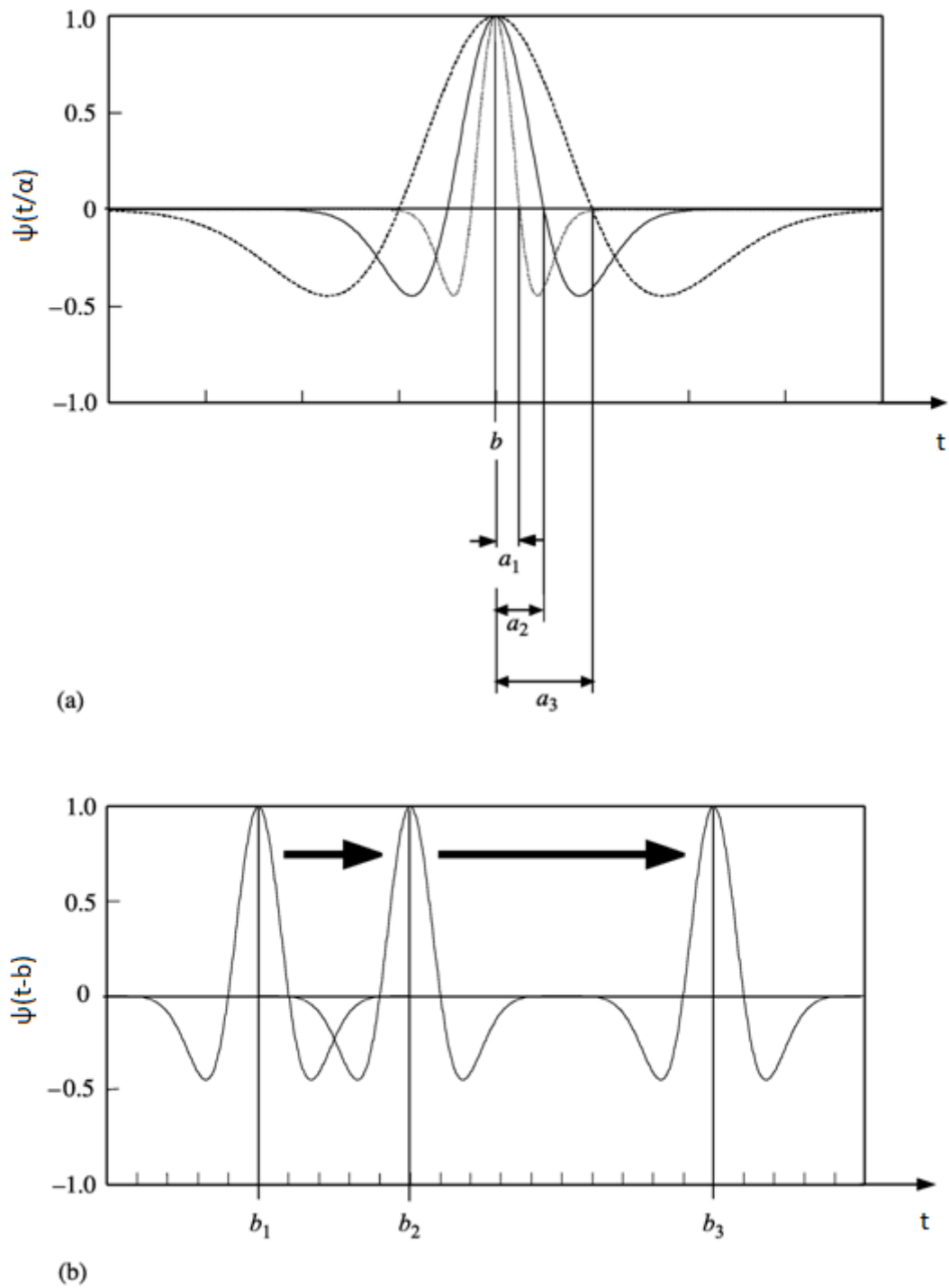


Figure 3.1 Dilation and translation of a wavelet. (a) Stretching and squeezing a wavelet: dilation ($a_1 = a_2/2$, $a_3 = a_2 \times 2$). (b) Moving a wavelet: translation.

3.2 Requirements For The Wavelet

$\psi(t)$ is the wavelet “mother” function that satisfies the constraints:

$$\int_{-\infty}^{+\infty} \psi(t) dt = 0 \quad (3.1)$$

In order for the transform to be invertible, the wavelet $\psi(t)$ must satisfy the admissibility condition [35]:

$$C_{\psi} = \int_{-\infty}^{+\infty} |\hat{\psi}(\omega)|^2 \frac{d\omega}{\omega} < +\infty \quad (3.2)$$

3.3 1-D Continuous Wavelet Transform

The continuous wavelet transform (CWT) is defined as follows:

$$WT(a, b) = \int_{-\infty}^{+\infty} f(t) \psi_{a,b}(t) dt \quad (3.3)$$

where,

$$\psi_{a,b}(t) = \frac{1}{\sqrt{a}} \psi\left(\frac{t-b}{a}\right) \quad (3.4)$$

is a window function called the mother wavelet a is a scale and b is a translation.

If $\hat{\psi}(\omega)$ is the Fourier transform of $\psi(t)$ and $f(\omega)$ the Fourier transform of $f(t)$ then:

$$\hat{WT}_a f(\omega) = \hat{\psi}(s\omega) f(\omega) \quad (3.5)$$

The function $f(t)$ can be reconstructed from its wavelet transform [35]:

$$WT^{-1} : f(t) = \frac{1}{C_{\psi}} \int_{-\infty}^{+\infty} \int_0^{+\infty} WT(a,b) \psi_{a,b}(t) \frac{dadb}{a^2} \quad (3.6)$$

There are, in fact, a large number of wavelets to choose from, for use in the analysis of our data. The best one for a particular application depends on both the nature of the signal and what we require from the analysis (i.e. what physical phenomena or

process we are looking to interrogate, or how we are trying to manipulate the signal). Some main wavelets you can see in the figure 3.2.

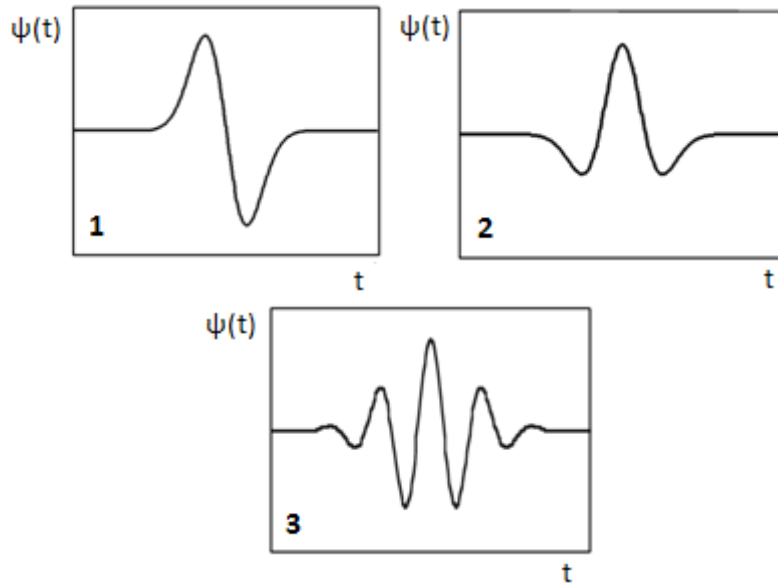


Figure 3.2. (1) Gaussian wave (first derivative of a Gaussian). (2) Mexican hat (second derivative of a Gaussian). (3) Morlet (real part).

3.4 2-D Continuous Wavelet Transform

The continuous wavelet transform of a 2D signal $f(t_1, t_2)$ is defined as [42]:

$$WT(a_1, a_2, b_1, b_2) = \int_{-\infty}^{+\infty} \int_{-\infty}^{+\infty} f(t_1, t_2) \bullet \psi(a_1, a_2, b_1, b_2, t_1, t_2) dt_1 dt_2 \quad (3.7)$$

Mother wavelet:

$$\psi(a_1, a_2, b_1, b_2, t_1, t_2) = \frac{1}{\sqrt{|a_1, a_2|}} \psi\left(\frac{t_1 - b_1}{a_1}, \frac{t_2 - b_2}{a_2}\right) \quad (3.8)$$

A reconstruction of the image can be achieved with the inversion formula:

$$WT^{-1} : f(t_1, t_2) = \frac{1}{C_\psi} \int_{-\infty}^{+\infty} \int_{-\infty}^{+\infty} WT(a_1, a_2, b_1, b_2) \psi(a_1, a_2, b_1, b_2, t_1, t_2) \frac{da_1 da_2}{|a_1 a_2|^2} db_1 db_2 \quad (3.9)$$

The admissibility condition (that allows to reconstruct the function f),

$$C_{\psi} \equiv 2\pi^2 \int_{-\infty}^{+\infty} |\hat{\psi}(\omega_1, \omega_2)|^2 \frac{d\omega_1 d\omega_2}{|\omega_1 \omega_2|} \quad (3.10)$$

Where $\hat{\psi}(\omega_1, \omega_2)$ represents the 2D Fourier transform of ψ and $||$ denotes the modulus of the complex number.

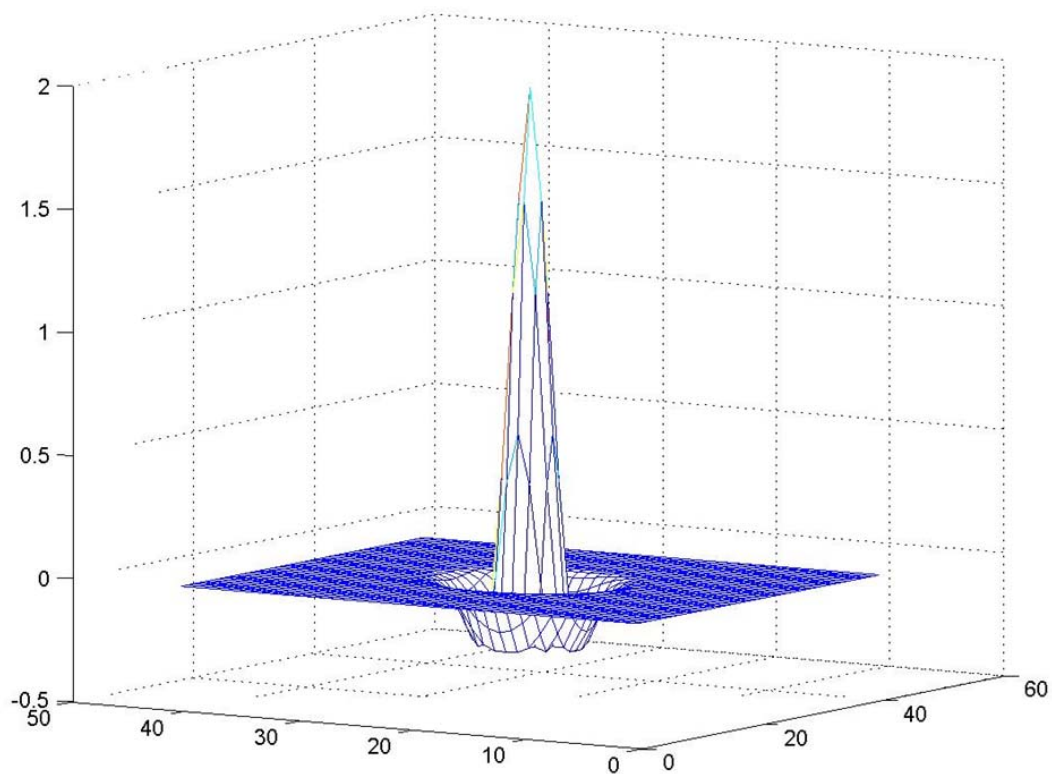


Figure 3.3 2D Mexican Hat wavelet.

CHAPTER 4

FAST AND ROBUST VESSEL LUMEN SEGMENTATION AND STRUT DETECTION IN INTRAVASCULAR OCT

Introduction

Optical Coherence Tomography (OCT) is a catheter-based imaging method that employs near-infrared light to produce high-resolution cross-sectional intravascular images. We propose a new segmentation technique for automatic lumen area extraction and stent strut detection in intravascular OCT images for the purpose of quantitative analysis of neointimal hyperplasia (NIH) and also we create a graphical user interface (GUI) for our code.

4.1 Previous Work

Few attempts have been made toward lumen segmentation in OCT images. Tanimote et al. [43] proposed a semiautomatic method that employs a combination of an edge detection filter and a smoothing operator so as to acquire the lumen area boundary in intracoronary arteries, both in vitro and in vivo. The introduced algorithm is based on the existing segmentation software named CURAD. [44] The user intervention includes the initialization of various starting points within the OCT image to ensure the correctness and the continuity of the extracted contour. Consensus in the measurements of two expert observers was reached with the use of intraclass and interclass correlation coefficients and the reliability coefficients. [45] The absolute and relative difference between lumen area measurements was $0.02 \pm 0.10 \text{ mm}^2$ and $0.3 \pm 0.5\%$, respectively.

Another edge detection technique in order to acquire the vessel lumen border for in vivo human coronary vessels was proposed by Sihan et al. [46] As a preprocessing step a despeckling filter is utilized to reduce speckle-noise and normalize gaps and shape irregularities in the vessel lumen interface. Subsequently, an iterative implementation of the Canny filter [47] via a binary search was employed, until the desired percentage of image pixels were classified as edge pixels. This classification

procedure between contour edges and the edges caused from noise or other structures within the OCT image was achieved by thresholding at first the dot product between the gradient orientation and catheter center, and afterward the edge length. The human observer measured a lumen area of $4.1 \pm 1.4 \text{ mm}^2$ while the proposed methodology calculated the same area as $4.0 \pm 1.3 \text{ mm}^2$ ($p=0.09$).

Endothelialization and NIH quantification in follow-up OCT images was also assessed throughout the past few years. Bonnema et al. [48] introduced a fully automatic method to detect covered and uncovered struts and establish a percent cellular coverage for a volumetric OCT dataset. The algorithm proposed, was evaluated in tissue-engineered human blood vessels. It comprises of three distinct steps. At first, the luminal surface is identified in an iterative process based on the maximum reflected intensity in order to isolate possible strut positions. Afterward, a strut detection algorithm is employed in which image pixels are considered as strut pixels if they satisfy three conditional characteristics: bright reflection at the surface of the strut, concentrated energy and a dark shadow underneath the strut. Finally, the difference between the luminal profile of the mimic and the position of the luminal strut surface is evaluated to determine the cellular coverage. Based on the manual assessment, the uncovered strut identification algorithm operated with a sensitivity of 93% and a specificity of 99%. In case of the struts inside the hyperplasia area the algorithm reached 81% sensitivity and 96% specificity.

Gurmeric et al. [49] also proposed an automatic stent implant follow-up in intravascular OCT images. The lumen extraction and strut detection was accomplished by a deformable spline contour model that propagates with ordinary differential equations toward an optimal solution. The percentage of correctly detected struts was calculated as the absolute difference between the number of struts marked by the physician and the number of struts detected by the proposed algorithm achieving an approximate accuracy of 86% in strut detection.

Kauffmann et al. [50] suggested an automatic and supervised lumen and strut detection algorithm to evaluate re-endothelialization in OCT images. The inner wall delineation is carried out in three consecutive steps: binarization of the OCT image using the Otsu method, [51] approximation of the wall border through

morphological segmentation and inner contour extraction via an initialization of active contour model near to real edges of the vessel. The strut detection procedure takes place via a gradient-based shadow detection algorithm and analyzing gray level radial profiles. The strut detection rate ranged from 35.42% to 73.39% in vivo and up to 84.44% in vitro acquisitions.

Unal et al. [52] recommended an automatic segmentation method in OCT images. The lumen segmentation is applied, in previously denoised images, throughout an active contour framework that employs two Catmull-Rom splines that are initialized by shooting rays from the center of each image to every direction. The strut detection is also based in shadow detection by analyzing angular intensity energy distribution in the lumen area. The mean difference between the computer method and expert evaluations for lumen cross-section area was $0.11 \pm 0.70 \text{ mm}^2$, $r^2=0.98$, $p<0.0001$. The average number of detected struts was 10.40 ± 2.90 per cross section when the expert identified 10.50 ± 2.80 , $r^2=0.78$, $p<0.0001$.

Both Unal et al. [52] and Gurmeric et al. [49] introduced for the first time computerized applications of the lumen- vessel border detection and strut detection to quantitatively assess stent endothelialisation and NIH development in-stent placement follow-up studies within intracoronary OCT.

An automated strut detection algorithm was also developed based on an adapted K-nearest neighbour method by Bruining et al [53]. The classification between struts or not in a polar transformed OCT image is employed with a modified K-nearest neighbour (mKNN) algorithm. The mKNN with a-priori information is applied to all rows to find a solution for this classification problem. The a-priori information consists of five manually selected frames that we considered visually diverse enough to detect most of the struts. Validation in just implanted stents group (n=15) resulted in a success rate of 77%. In a stent follow-up group (n=14) 6 months after implantation with tissue growth inside a success rate of 50% was observed.

Tsantis et al [54] proposed a segmentation technique for automatic lumen area extraction and stent strut detection in intravascular OCT images for the purpose of quantitative analysis of neointimal hyperplasia (NIH). A clinical dataset of frequency-domain OCT scans of the human femoral artery was analyzed. First, a segmentation

method based on the Markov random field (MRF) model was employed for lumen area identification. Second, textural and edge information derived from local intensity distribution and continuous wavelet transform (CWT) analysis were integrated to extract the inner luminal contour. Finally, the stent strut positions were detected via the introduction of each strut wavelet response across scales into a feature extraction and classification scheme in order to optimize the strut position detection. Results: The inner lumen contour and the position of stent strut were extracted with very high accuracy. Compared with manual segmentation by an expert vascular physician the automatic segmentation had an average overlap value of 0.937 ± 0.045 for all OCT images included in the study. The strut detection accuracy had an area under the curve (AUC) value of 0.95, together with sensitivity and specificity average values of 0.91 and 0.96, respectively.

Lu et al [55] developed a highly automated method for detecting stent struts and measuring tissue coverage. A bagged decision trees classifier was employed to classify candidate struts using features extracted from the images. Strut detection statistics approached variability of manual analysis. Differences between manual and automatic area measurements were $0.12 \pm 0.20 \text{ mm}^2$ and $0.11 \pm 0.20 \text{ mm}^2$ for stent and tissue areas, respectively.

Most aforementioned approaches [43,44,46–50,52] either employed only edge detection techniques with ad hoc thresholding, or more complex approaches with active or spline deformable models that are mainly intensity-based. It is worth mentioning that they do not clarify how they encounter the bright concentric rings that apparently would decrease the active contour model performance. The complex nature of OCT imaging make strut detection as one of the most challenging tasks among medical image processing applications. Different reflection angles, refraction phenomena, misplaced probe positions together with speckle noise, altering continuously the strut reflection surface. Therefore, detection approaches that do not integrate these complex characteristics are most likely to have limited performance. Strut detection algorithms [48,49,50,52] published so far, consider as prerequisite the fact that behind the strut bright surface a shadow area is created due to high reflectivity. However, this is not always the case since in many occasions

bright surfaces can be present without shadowing. In addition, in several OCT images struts are partially or totally invisible leaving a comet tail behind.

4.2 Oct Clinical Dataset

For this study, Fourier domain OCT (FD-OCT) of the femoral artery was performed with a commercially available system (C7-XR, Lightlab, Massachusetts, USA). OCT acquisitions were performed with a dextrose saline flush (glucose 5%w/v) technique with simultaneous manual obstruction of the common femoral artery. Routine OCT acquisitions during follow-up of femoral arteries with previously implanted stents were employed. Stents examined were commercially available new generation nitinol self-expanding stents that are approved for the femoral artery. Femoral nitinol stents expand up to a 5–7 mm diameter once implanted due to their thermal memory properties, the stent mesh is produced with laser-cutting technology in variable lengths (up to 20 cm) and they have an almost square sub-millimeter cross-sectional stent strut configuration.

Four OCT in vivo sequences of the human femoral artery (each scan visualizing 54 mm of vessel lumen in 270 consecutive frames; 1080 frames analyzed in total) were included in the study for the vessel lumen border extraction algorithm. Stent struts because of previous stent placement were identified in all 4 femoral OCT sequences. However, individual stent struts were present in 300 frames from all sequences and were further included in the strut detection study. The OCT unit performs automatic or manual calibration every time before study acquisition against an item of known size (i.e., the size of the catheter used $\approx 2.7\text{Fr} = 0.9\text{ mm}$) [56, 57]. This unit is also digital imaging and communications in medicine (DICOM) compliant and thus exported images contain all calibration information (e.g., pixel size) needed to produce quantitative results. Calibration was also checked before quantitative analysis. OCT acquisition parameters are outlined in detail in Table 1.

TABLE 5.1. FD-OCT scan parameters of the femoral artery.[58]

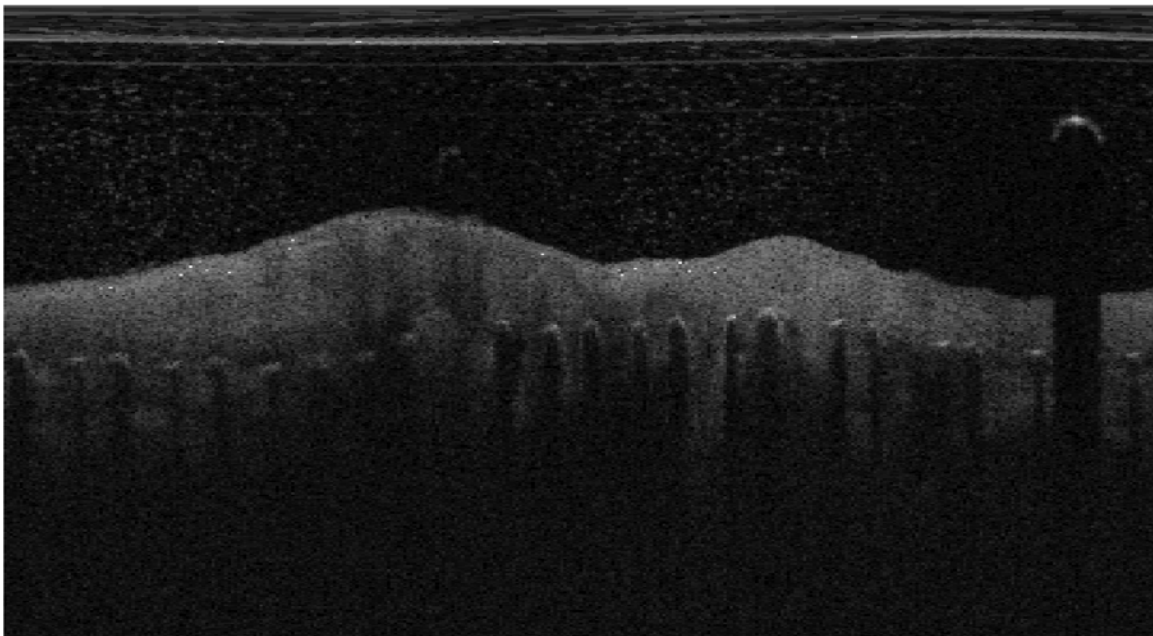
OCT technology	Frequency-domain image reconstruction
OCT catheter	Monorail optical fiber (C7-XR, Lightlab, Massachusetts, USA)
Guide wire size	0.01400 compatible
Working channel	3.7Fr (0.01400 wire plus the catheter with the optical fiber)
Injector pump	Automated electronic injector (Medrad, Warrendale, USA)
Flush technique	50 ml of dextrose 5%w/v at 10ml/s (max 400psi)
Light wavelength	1250–1350nm
Axial resolution	15–20 μ m
Lateral resolution	25–200 μ m (depending on pullback speed)
Scan diameter	3–8 mm (8.3 mm in saline)
Max pullback speed	20 mm/s
Acquisition length	54 mm
Acquisition time	2.7 s
Frame rate	100 f/s
Number of frames	270
Image export format	DICOM

4.3 Lumen Wall Delineation

Before applying the combined FCM and CWT algorithms each OCT frame is transformed from the Cartesian coordinates (x,y) consisting of 1024×1024 pixels (pixel size 7 by 7 mm) to the polar coordinates (r,θ) in which the horizontal and vertical axes represent, respectively, the angular position between 0 and 360 and the pixel position from image center (probe position) to image border (Figure 5.1).



(a)



(b)

Figure 5.1 (a) Typical OCT image, (b) Polar reformation of the OCT image in which the horizontal and vertical axes represent, respectively, the angular position (θ : $0^\circ - 360^\circ$) and the pixel position from image center to image border (r : 1 – 512 pixels).

The Cartesian coordinates x and y can be converted to polar coordinates r and ϑ with $r \geq 0$ and ϑ in the interval $(-\pi, \pi]$ by [59]:

$$r = \sqrt{x^2 + y^2} \text{ (as in the Pythagorean theorem)} \quad (4.1)$$

and

$$\theta = \arctan 2(x, y) \quad (4.2)$$

Then to construct the image as we see in figure 5.1 b) we use the following equations:

$$x = x_0 + r \cos(\theta) \quad (4.3)$$

and

$$y = y_0 + r \sin(\theta) \quad (4.4)$$

Where x_0, y_0 is the center of the OCT (1024x1024) images.

The FCM algorithm assigns pixels to two or more clusters by using fuzzy memberships [Bezdek *et al*]. It is considered as an iterative optimization that minimizes a cost function when pixels close to the centroid of their clusters, are assigned with high membership values. This membership function represents the probability that a pixel belongs to a specific cluster. Let $V = \{v_1, v_2, \dots, v_n\}$ denotes an image with N pixels to be partitioned into $c = 2$ (i.e. the lumen and the hyperplasia area) clusters, where x_j represents the feature value. The cost function is defined as follows:

$$Q_{fcm} = \sum_{j=1}^n \sum_{i=1}^C \mu_{ij}^m \|v_j - \mu_i\|^2 \quad 1 \leq m < \infty \quad (4.5)$$

subject to:

$$\sum_{i=1}^c u_{ij} = 1, \quad u_{ij} \in [0,1], \quad 1 \leq j \leq n, \quad 1 \leq i \leq c \quad (4.6)$$

Where $m \in (1, \infty)$ controls the fuzziness of the resulting partition, u_{ij} and $d_{ij}^2 = \|v_i - \mu_i\|^2$ represent the membership of pixel v_i in the i th clustering, and the distance between the pixel v_i and the cluster center μ_i respectively. In image clustering, the most commonly used feature is the gray-level value, or intensity of image pixel. Thus the FCM cost function is minimized when high membership values are assigned to pixels whose intensities are close to the centroid of their clusters and low membership values are assigned when the point is far from the centroid. The membership function represents the probability that a pixel belongs to a specific cluster. In the FCM algorithm, the probability is dependent solely on the distance between the pixel and each individual cluster center in the feature domain. The membership function and cluster centers are updated by the following:

$$u_{ij}^m = \frac{1}{\sum_{k=1}^c \left(\frac{\|v_j - \mu_i\|}{\|v_j - \mu_k\|} \right)^{\frac{2}{m-1}}} \quad (4.7)$$

$$\mu_i = \frac{\sum_{j=1}^n u_{ij}^m v_j}{\sum_{j=1}^n u_{ij}^m} \quad (4.8)$$

Starting with an initial guess for each cluster center, the FCM converges to a solution for μ_i representing the local minimum or a saddle point of the cost function. Convergence can be detected by comparing the changes in the membership function or the cluster center at two successive iteration steps.

The continuous wavelet transform (CWT) provides a time-frequency representation of a signal offering time and frequency localization. The wavelet coefficients $Wf(b, \alpha)$ of the CWT are provided by convolving the signal $f(t)$ with shifting by b and scaling by a family of functions ψ [60]:

$$Wf(b, a) = |a|^{-1} \int_{-\infty}^{+\infty} f(t) \psi\left(\frac{(t-b)}{a}\right) dt \quad (4.9)$$

In this study, the 2D CWT was implemented employing the “Mexican hat” wavelet filter [61]:

$$\psi(t) = \frac{2}{\sqrt{3\sigma\pi^{1/4}}} \left(1 - \frac{t^2}{\sigma^2}\right) e^{-\frac{t^2}{2\sigma^2}} \quad (4.10)$$

which is the normalized negative second derivative of a Gaussian function (equivalent to the Laplacian Of Gaussian– LOG function). The 2D wavelet coefficients $Wf(a_1, a_2, b_1, b_2)$ of an image $f(t_1, t_2)$ are defined as:

$$Wf(a_1, a_2, b_1, b_2) = |a_1 a_2|^{-1} \int_{-\infty}^{+\infty} f(t_1, t_2) \bullet \psi\left(\frac{t_1 - b_1}{a_1}, \frac{t_2 - b_2}{a_2}\right) dt_1 dt_2 \quad (4.11)$$

The FCM algorithm determines the centroids and membership function pixel-by-pixel while it is employed for image clustering. In addition, FCM is considered as a local search optimization algorithm, and due to this it is very sensitive to the initial centroid. If the initial centroid is generated randomly, it is possible that the convergence of the algorithm will become time-consuming which turns out to be impractical for image clustering purposes. So as to avoid the blindness of random evaluation and processing time increment, CWT analysis provides the initial centroids in order to minimize the number of iteration steps. This initialization step provides edge information into the FCM clustering algorithm by selecting the initial centroid from the gray values that correspond to high wavelet coefficient values that represent the maximum optical intensity difference between the pixels from the vessel and luminal side along the contour. Consequently the FCM algorithm divides the OCT image data into the two final clusters (i.e., one cluster concerning the area that presents with a high light reflectance and a second cluster concerning the areas in the image with a low light reflectance) figure 5.2. The vessel lumen boundary provided from the clustered image in Cartesian coordinates is depicted in Figure 5.3

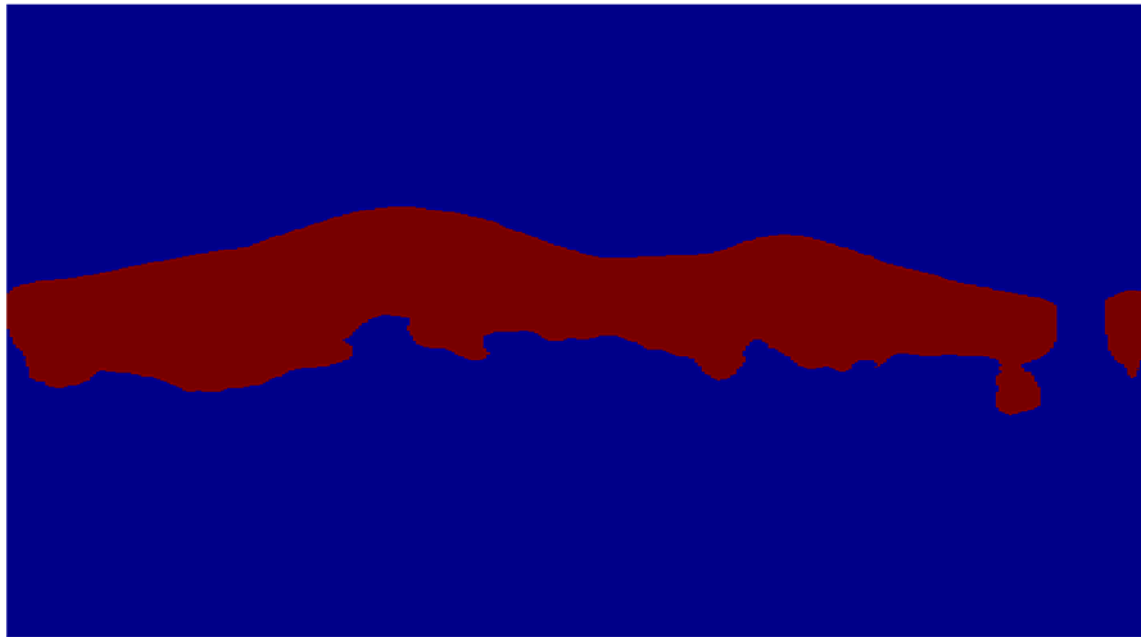


Figure 5.2. FCM combined with CWT clustering. Red area represents the vessel wall in polar coordinates.

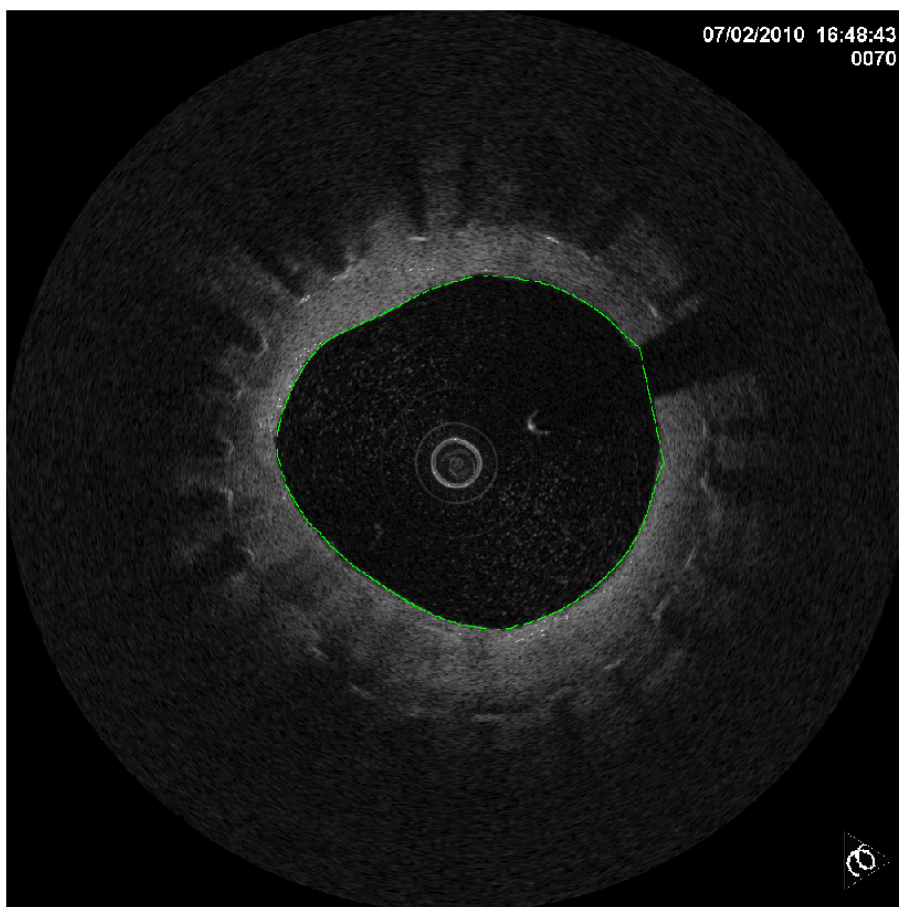


Figure 5.3. Vessel Lumen border delineation

In practice, the clustering program is stopped if the convergence error is smaller than 10^{-3} or 100 iterations are achieved. Due to the wavelet transform initialization the average number of iterations was approximately 3. The fuzziness value was set at $m=2$ in this study to further reduce the computation time (the power functions are replaced by squares).

In order to evaluate the clustering performance of the proposed method, a comparative study has been held between the clustering results and the “ground truth” derived from an expert physician who manually delineated the lumen area, by means of overlap degree between the two sets. Overlap is defined as the ratio of intersection over the union of the two clustered areas [62]. The value of overlap is bound between zero (no overlap) and one (exact overlap).

4.4 Stent Strut Position Detection

In OCT images, stent struts do not have a constant appearance. They often give a bright reflection and usually appear as small line segments or spots depending on the light reflection angle. In some cases they also they produce a shadow zone behind the bright echo. The proposed algorithm approaches the strut position detection as a blob detection procedure in which blobs are considered as the maximum response of the LOG filter in the CWT analysis. All wavelet local maxima values that correspond to various structures within the OCT image are considered as candidate strut positions.

In cases where most of the strut is visible the corresponding wavelet local maxima can be discriminated from other structures within the OCT image. However, in most cases the transmission – reflection light path is not perpendicular and produces a shortened line segment or a small blob with lower brightness values. This is due to refraction of the incident light beam. This complexity of OCT images enhances the strut pattern variability, which in turn constitutes the edge information provided by the wavelet coefficient values as insufficient information towards accurate strut detection. In order to overcome the aforementioned limitations a new map has been built that incorporates the edge properties provided by the wavelet local maxima value combined with spatial and regional properties of the strut.

Although the wavelet values are similar, there are spatial (size of the structure) and regional (adjacent structural environment) properties that can distinguish the correct strut positions. A thorough examination has been made in order to quantify these properties so as to discriminate the strut responses from the other candidate positions. The candidate strut positions are located either in the interface between lumen and vessel area or within the hyperplasia area. The alteration of size and neighborhood of each candidate maxima position consequently transforms the size and behavior of each wavelet response (Figure 5.3).

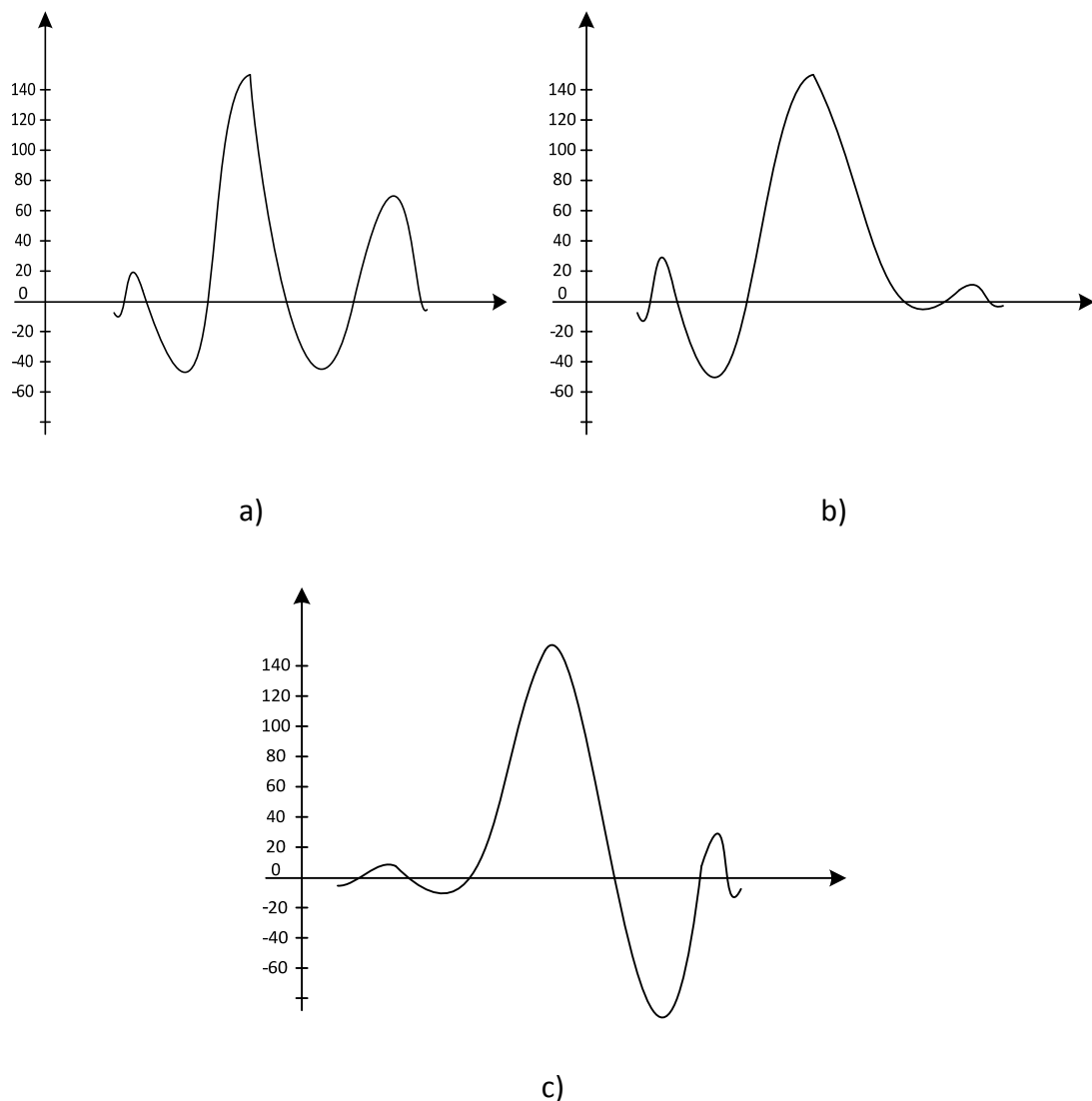


Figure 5.3 Wavelet signal transitions of various structures located as local maxima within the OCT image. (a) Strut response, (b) response in lumen/vessel wall points, (c) other response within the vessel that does not correspond to strut.

Two metrics have been employed towards the new mapping, the Full Width Half Maximum – U_1 (FWHM) that represents the spatial resolution properties of each strut and the relation between the corresponding wavelet signal transitions starting at a local minimum, followed by the local maximum and ending again at a local minimum – U_2 (figure 5.4).

$$U_1 = FWHM \quad (4.12)$$

$$U_2 = \frac{max - min_2}{max - min_1} \quad (4.13)$$

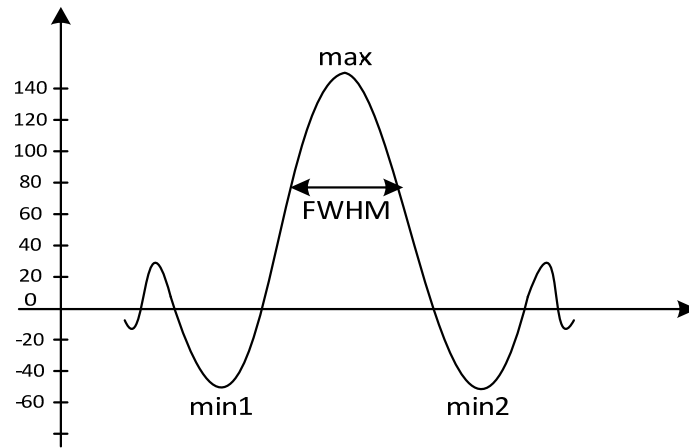


Figure 5.4 Wavelet transform response of a candidate strut position and the metrics employed towards strut detection procedure.

The FWHM metric emerges the size differentiation of each candidate maxima. Apparently struts are thinner than the other structures providing smaller FWHM values. Also U_2 metric due to the signal transition bilaterally from the maxima provides the symmetry response thus revealing the homogeneity environment around the strut positions within the hyperplasia. A symmetrical (value close to 1) response suggests a strut covered with hyperplasia.

Each wavelet local maxima is transformed into the new mapping value with the following equation:

$$U = U_2 * \frac{LocalMaximavalue}{U_1} \quad (4.14)$$

The new map values are utilized to the FCM membership function providing high membership values for strut wavelet responses and low memberships values for the rest of the wavelet responses (Figure 5.5, figure 5.6).

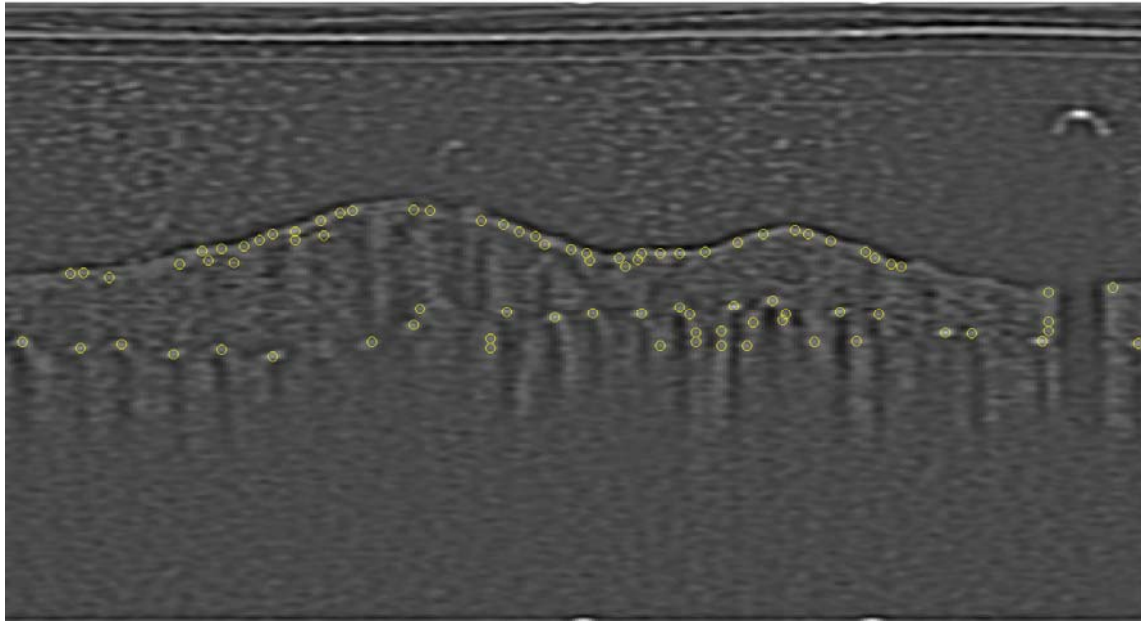


Figure 5.5 Wavelet edge map. Candidate strut positions (yellow circles) correspond to wavelet local maxima values.

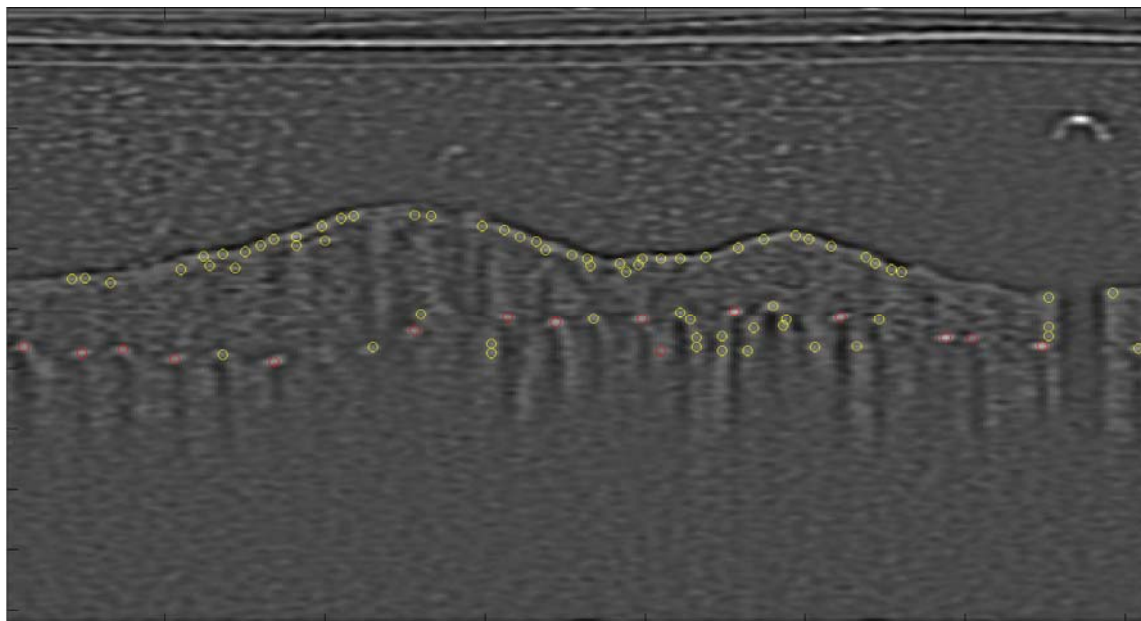


Figure 5.6 FCM clustering results from the new map. Red circles are clustered as struts whereas yellow as non-struts.

4.5 Hyperplasia Estimation

In order to approximate the hyperplasia extent a double fitting scheme with a feedback procedure is employed towards the hyperplasia quantification. The double fitting procedure inserts all wavelet local maxima clustered as struts into a gradient-weighted algebraic fitting algorithm so as to decide whether the struts points form a circle or an ellipse.

The circle algebraic fitting algorithm is based on the minimization of the sum of squares of algebraic distances from the circle with center (a,b) and radius R to the N data points x_i [63, 64]. The circle objective function F with the natural parameters is given:

$$F(a, b, R) = \sum_{i=1}^n [(x_i - a)^2 + (y_i - b)^2 - R^2]^2 \quad (4.15)$$

Where $a \neq 0$ and $b, c \in R^2$

The parameterized form is given by:

$$F(A, B, C, D) = \sum_{i=1}^n (Az_i + Bx_i + Cy_i + D)^2 \quad (4.16)$$

Where $A = 1$, $z_i = x_i^2 + y_i^2$, $B = -2a$, $C = -2b$ and $D = a^2 + b^2 - R^2$, under the constraint $B^2 + C^2 - 4AD = 1$. Every circle will correspond to a unique quadruple (A, B, C, D) and vice versa.

In order to approximate the local maxima points clustered as struts the implicit polynomial function $P(x,y)=0$ that describes a circle is minimized. The coefficients of the polynomial are equivalent with the aforementioned parameters. The gradient weighted algebraic fit is based on minimizing:

$$F_g = \sum_{i=1}^n \frac{[P(x_i, y_i)]^2}{\nabla[P(x_i, y_i)]^2} \quad (4.17)$$

Where $P(x, y) = A(x^2 + y^2) + Bx + Cy + D$.

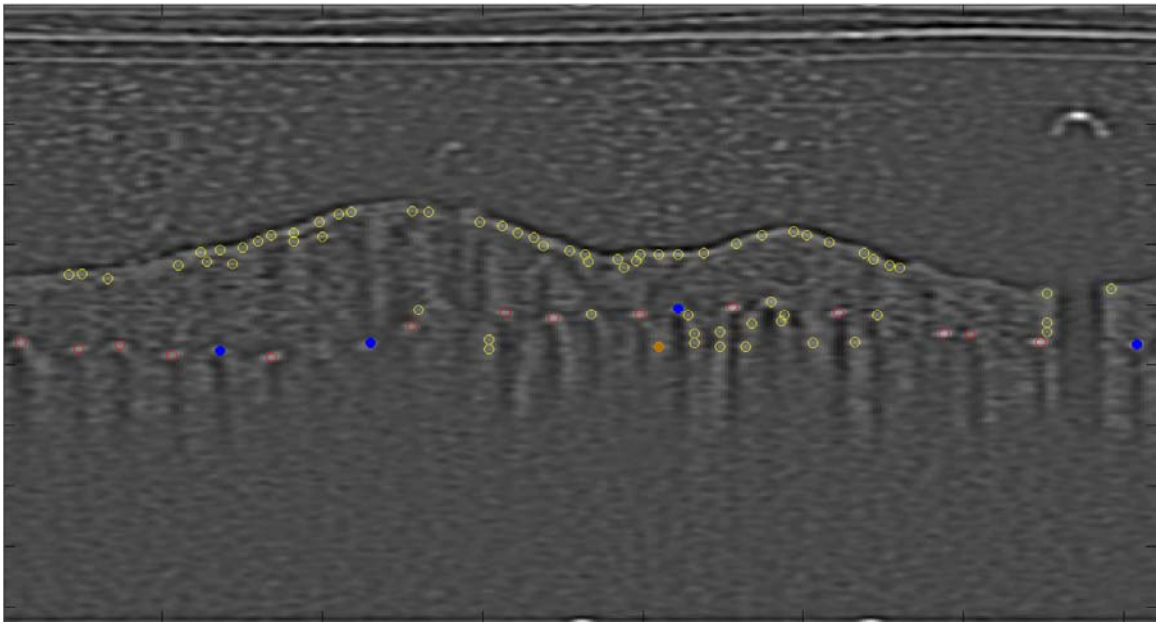
The ellipse fitting algorithm considers the implicit quadratic polynomial function that represents a general conic [64]:

$$F(A, X) = A \cdot X = ax^2 + bxy + cy^2 + dx + ey + f \quad (4.18)$$

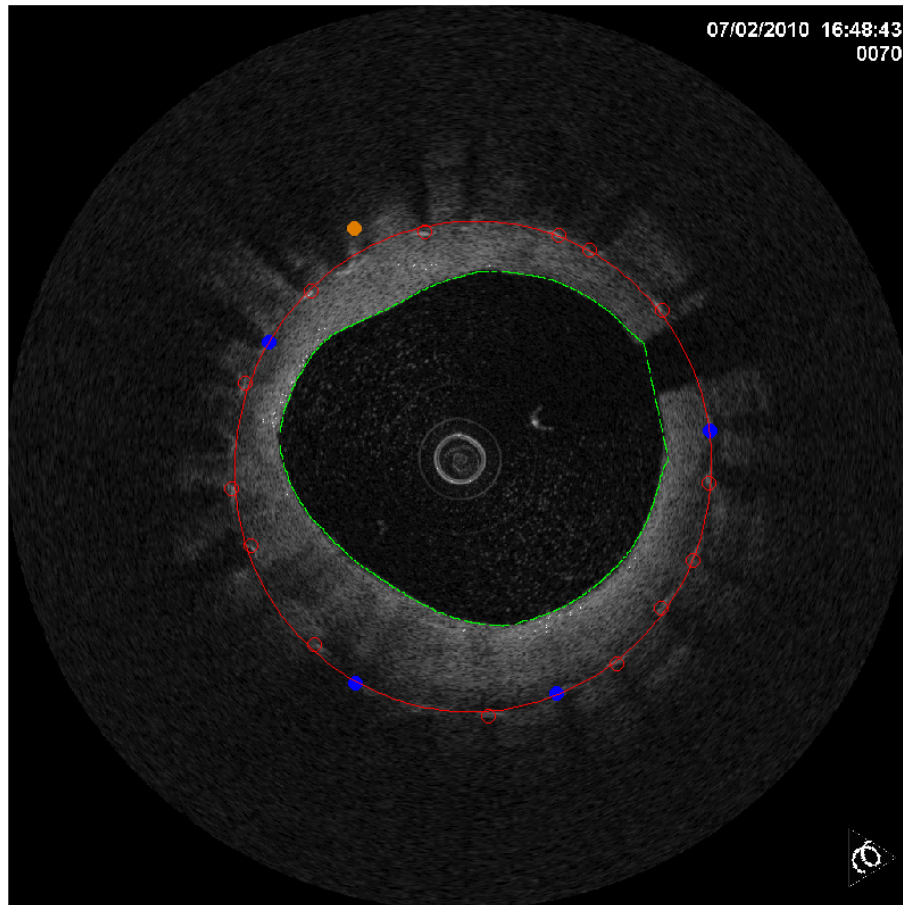
Where $A = [abcdef]^T$ and $X = [x^2xyy^2xy]$. $F(A; X_i)$, is called the algebraic distance of a point (x, y) to the conic $F(A; X_i) = 0$. The fitting is approached by minimizing the sum of squared algebraic distances:

$$D(A) = \sum_{i=1}^N F(X_i)^2 \quad (4.19)$$

The best fit between the two aforementioned algorithms is considered as the curve with the minimum distance between the approximated curve points and the local maxima points. A feedback algorithm is also employed towards the optimization of the strut detection procedure. All local maxima points (struts and not struts) are re-inserted in the best fitting curve computed from the preceding step to check any possible misclassifications from the FCM clustering. Any misclassified point of either cluster that fits the approximated curve (circle or ellipse) is classified to the correct group (Figure 5.7).



(a)



b)

Figure 5.7 Double fitting procedure with feedback procedure towards hyperplasia quantification. (a) the fitting procedure adds in the strut group four additional points (blue dots) missed by the FCM clustering whereas removes a false classified point as strut (orange dot) in polar coordinates. (b) The fitting algorithm in Cartesian coordinates.

The fitting procedure besides the hyperplasia quantification increases the specificity of the proposed method by reducing the number of false maxima classified as struts combined with the sensitivity increment by adding in the struts cluster any maxima that was missed from the FCM algorithm.

4.6 Quantitative Results

Regarding the inner vessel lumen segmentation accuracy, the overlap degree results provided by the proposed method are at first compared with manual segmentation by an expert physician in terms of overlap degree between the two sets. The proposed automatic segmentation had an average overlap value of 0.917 ± 0.065 for all OCT images included in the study.

Also the proposed method and all automatic segmentation algorithms utilised in this thesis such as k-means, Fcm, MRF – lcm and MRF – Metropolis were compared by means of mean distance difference in mm and processing time in sec with the physician's manual assessments. Table 5.2 gives a detailed account of the performance differences between the clustering algorithms.

TABLE 5.2 Quantitative results. Values expressed as means in mm and in sec.

	Mean Difference Distance(mm)	Processing Time (s)
Proposed Method	0,09170	5,1
FCM	0,09398	8,2
K-means	0,09544	8,7
MRF – lcm	0,08996	11,6
MRF – Metropolis	0,08888	12,9
S. Tsantis et al	0,08714	14,8

Regarding the strut detection procedure, Table 5.3 gives a detailed account of the strut detection accuracies obtained by the proposed method. The strut detection procedure successfully identified 9.57 ± 0.5 struts for each OCT image.

TABLE 5.3 Truth Table of the strut detection procedure

Local Maxima	Strut Detection		
	Rest	Strut	
Rest	22398	848	96.35%
Strut	821	2868	77.74%
Overall Accuracy			93.80%

The accuracy values presented in Table 5.3 are calculated after the double fitting algorithm employment. The corresponding values before the fitting algorithm were 89.77% as overall accuracy with sensitivity and specificity values of 66.00% and 94.07% respectively. These results are highly indicative of the effectiveness of the

proposed method towards an accurate strut detection procedure. After algorithmic application toward detection of the lumen area and stent struts in each one of the four femoral OCT datasets, the following parameters indicated as clinically significant by the team of interventional radiologists were calculated in every OCT frame; maximum stent diameter (D_s ; corresponding to vessel diameter immediately after stent placement), maximum lumen diameter (D_L ; corresponding to the maximum patent lumen diameter at the time of the OCT acquisition after development of NIH), late lumen loss (D_{LLL} ; corresponding to the maximum thickness of NIH), stent area (A_s ; corresponding to cross-sectional vessel area immediately after stent placement), and lumen area (A_L ; corresponding to cross-sectional patent lumen area at the time of the OCT acquisition after development of NIH) (Fig. 5.8).

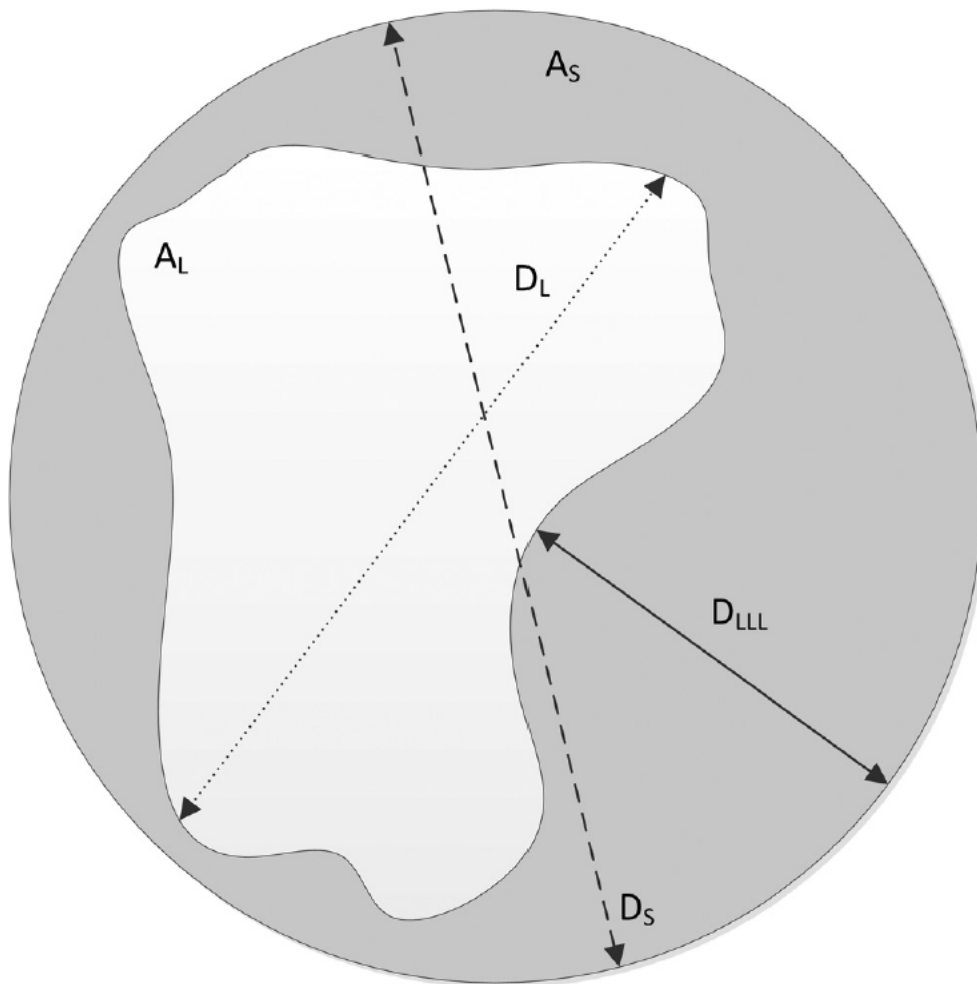


Figure 5.8 Typical OCT frame graphical reproduction with the different calculated lengths and areas; D_s , D_L , D_{LLL} , A_s , and A_L

Quantitative data after calculation of the predetermined morphological variables in the four individual clinical data sets are outlined in detail in Table 5.4.

TABLE 5.4 Quantitative results. Values expressed as means (standard deviation).

	Maximum Stent Diameter Ds (mm)	Maximum Lumen Diameter Dl(mm)	Diameter Stenosis Dst%	Late Lumen LossDIII(mm)	Stent Area As (mm ²)	Lumen Area Al (mm ²)	Area Stenosis Ast%	Neointimal hyperplasia Area (mm ²)
Case 1	6,04(0.10)	2,17(0.25)	20,69(5.12)	0,52(0.15)	5,82(0.41)	3,37(0.72)	42,04(3.24)	2,45(2.58)
Case 2	3,49(0.22)	2,83(0.17)	19,14(6.2)	0,60(0.15)	7,91(1.09)	5,06(0.58)	35,93(2.58)	2,84(1.35)
Case 3	3,75(0.09)	2,86(0.15)	23,88(5.4)	0,75(0.08)	10,96(0.46)	5,95(0.6)	45,75(5.51)	5,01(0.88)
Case 4	3,34(0.18)	1,97(0.16)	15,75(4.3)	0,39(0.09)	4,11(0.5)	2,66(0.44)	35,32(3.01)	1,45(0.86)

Maximum stent diameter (DS) ranged from 3.34 to 6.04 mm, maximum lumen diameter DL from 1.97 to 2.86 mm, and late lumen loss(DLLL) was variable ranging from 0.39 to 0.75 mm. A wide range of vessel stenosis on a diameter or area basis (%Dstenosis ranged from 15.75% to 20.69%, while %Asthenosis ranged from 35.32% to 45.75%, respectively) was found in all analysed vessel segments. NIH had developed diffusely in all femoral arteries and the respective area ranged from 1.45 to 5.01mm².

4.7 Graphical User Interface Implementation

A GUI (Graphical User Interface) has been implemented towards employment of the proposed algorithm in a daily clinical practice. The GUI implemented performs the following functions:

- Load images
- Inner lumen contour extraction
- Strut contour extraction and struts finding
- Manual strut position correction

Each OCT image is loaded by pushing the “load image” push-button. The initial image appears in the first axis (right of the push-button “load image”).Afterwards the inner lumen contour is calculated (by pushing the “inner boundary” push-button).Also the strut contour along with the struts are visualised [it also keeps the inner contour “on”] (by pushing the “in out boundary strut” push-button). In that case they both appear in the second axis (right of the push-buttons “inner boundary”, “in out boundary strut”). The user has the possibility, if he is not satisfied with the final

result, to delete points that the algorithm considers wrongly as struts or add some that the algorithm does not found, by choosing add or remove from the pop-up menu. When all correction have been made, the “final” (push-button) should be pushed and the final result appears in axis 2. There are two static texts that help the user to interact better with the gui. When one of the two options is chosen the pop-up menu opens a big window, with the image enlarged so that we have better visual interpretation in the option of removal or adding of the struts, also in the same window appears a text that contains useful guidelines in order to choose the extra points. Finally the gui window has the potential to be resizable. Finally, all calculated parameters are saved for each OCT image in an excel file.

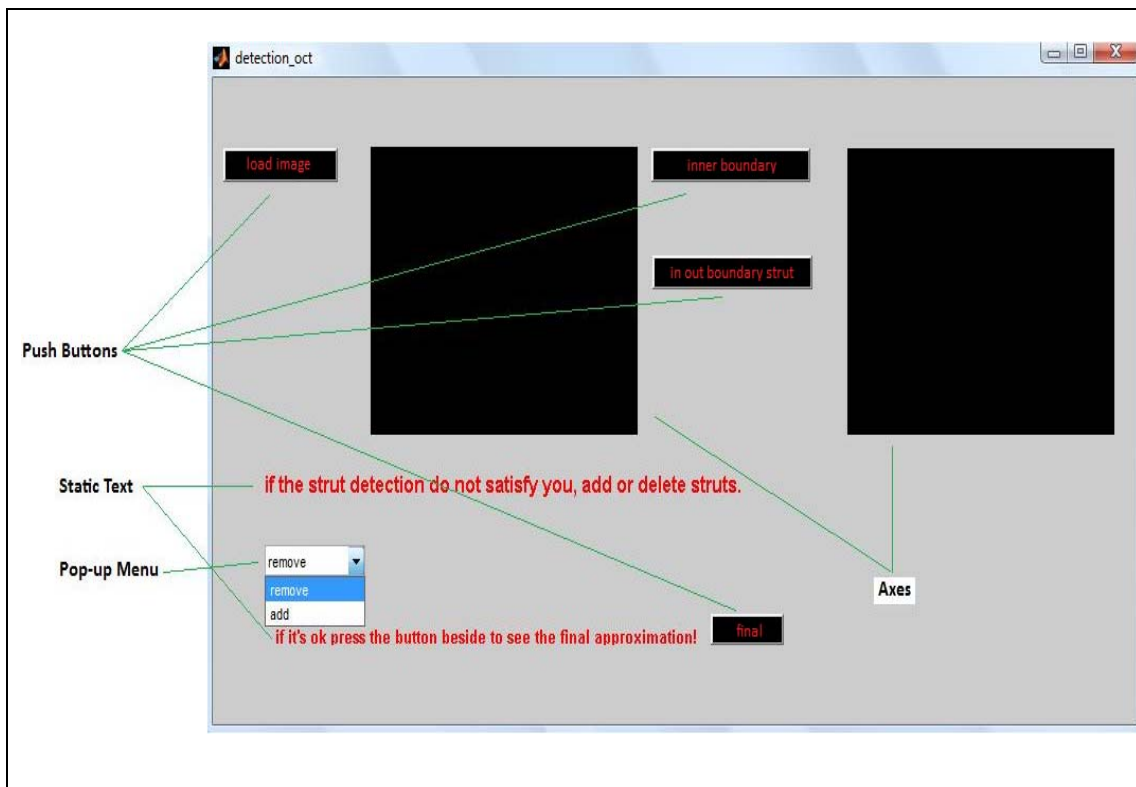


Figure 5.9 Graphical User Interface environment of the proposed method

4.8 Discussion

In the present thesis, a methodology is proposed to: (a) segment the vessel lumen border from 2D OCT images (via a combined scheme of an FCM model and CWT analysis) and (b) detect the positions of stent struts within the 2D OCT images (by utilizing metrics derived from the local maxima of the wavelet transform into the FCM membership function) in order to assess the degree of neointimal hyperplasia within the stented vessels from OCT images. More specifically, the vessel lumen border of the OCT images is extracted, and then, the stent struts within the images are detected. This study has the benefits that: (i) it gives quantitative information about NIH and (ii) it uses strut characteristics in order to classify whether areas of the OCT image belong to stent struts or not.

The complex nature of OCT imaging make strut detection as one of the most challenging tasks among medical image processing applications. Different reflection angles, refraction phenomena, misplaced probe positions together with speckle noise, altering continuously the strut reflection surface. Therefore, detection approaches that do not integrate these complex characteristics are most likely to have limited performance. Strut detection algorithms published so far, consider as prerequisite the fact that behind the strut bright surface a shadow area is created due to high reflectivity. However, this is not always the case since in many occasions bright surfaces can be present without shadowing. In addition, in several OCT images struts are partially or totally invisible leaving a comet tail behind. The proposed study throughout CWT analysis identifies sharp variations with great accuracy wherever they occur within the OCT image and consider them initially as candidate strut positions.

The strut detection accuracy of the proposed algorithm was significantly high reaching an overall accuracy value of 93.8%, together with high sensitivity and specificity values (averages of 77.74 % and 96.35%, respectively). Of further interest, the developed algorithm runs in an unsupervised fashion and demonstrated a robust performance in automatic vessel lumen segmentation and stent strut detection as shown by its pilot application in ten clinical datasets. The algorithm may prove

extremely useful in quantitative assessment of stent endothelialisation and NIH development in longitudinal studies of stent placement in the peripheral arteries. The software may accurately calculate late lumen loss and NIH area through-out the examined stent, thereby providing quantitative surrogate markers of vascular restenosis and vessel wall response after stent implantation.

REFERENCES

- [1] Huang D., Swanson E.A., Lin C.P., Schuman J.S., Stinson W.G., Chang W., Hee M.R., Flotte T., Gregory K., Puliafito C.A., Fujimoto J.G., Optical coherence tomography. *Science*, 1991. 254(5035): p. 1178–1181.
- [2] James G. FUJIMOTO Optical coherence tomography. *Applied physics*, 2001. 4 p. 1099–1111
- [3] Takada K., Yokohama I., Chida K., Noda J., New measurement system for fault location in optical waveguide devices based on an interferometric technique. *Applied Optics*, 1987. 26(9): p. 1603–1608.
- [4] Youngquist R.C., Carr S., Davies D.E.N., Optical coherence-domain reflectometry: a new optical evaluation technique. *Optics Letters*, 1987. 12(3): p. 158–160.
- [5] Gilgen H.H., Novak R.P., Salathe R.P., Hodel W., Beaud P., Submillimeter optical reflectometry, *IEEE J. Lightwave Technology*, 1989. 7(8): p. 1225–1233.
- [6] Fercher A.F., Mengedoht K., Werner W., Eye-length measurement by interferometry with partially coherent light. *Optics Letters*, 1988. 13(3): p. 1867–1869.
- [7] Huang D., Wang J., Lin C.P., Puliafito C.A., Fujimoto J.G., Micron-resolution ranging of cornea and anterior chamber by optical reflectometry. *Lasers in Surgery and Medicine* 1991 11(5): p. 419–425.
- [8] Regar, E., et al., Optical coherence tomography. *Cardiovasc Radiat Med*, 2003. 4(4):p. 198-204.
- [9] Yun, S., et al., High-speed optical frequency-domain imaging. *Optics Express*, 2003.11: p. 2953-2963.
- [10] Chinn, S.R., E.A. Swanson, and J.G. Fujimoto, Optical coherence tomography using a frequency-tunable optical source. *Optics Letters*, 1997. 22(5): p. 340-342.
- [11] Rollins, A.M., et al., In vivo video rate optical coherence tomography. *Optics Express*, 1998. 3(6): p. 219-229.

- [12] Leitgeb, R., C.K. Hitzenberger, and A.F. Fercher, Performance of fourier domain vs. time domain optical coherence tomography. *Optics Express*, 2003. 11(8): p. 889-894.
- [13] Choma, M., et al., Sensitivity advantage of swept source and Fourier domain optical coherence tomography. *Opt. Express*, 2003. 11(18): p. 2183-2189.
- [14] de Boer, J.F., et al., Improved signal-to-noise ratio in spectral-domain compared with time-domain optical coherence tomography. *Optics Letters*, 2003. 28(21): p. 2067- 2069.
- [15] Yun, S.H., et al., Comprehensive volumetric optical microscopy in vivo. *Nat Med*, 2006. 12(12): p. 1429-1433.
- [16] Lim, H., et al., High-speed imaging of human retina in vivo with swept-source optical coherence tomography. *Optics Express*, 2006. 14(26): p. 12902-12908.
- [17] Bock, H. H., *Automatische Klassifikation*. Vadenhoeck & Ruprecht, Göttingen, Zürich, 1974.
- [18] A.K. Jain, R.C. Dubes, *Algorithms for Clustering Data*, Prentice-Hall, Englewood Cliffs, NJ, 1988.
- [19] S. Theodoridis, K. Koutroumbas, *Pattern Recognition*, Elsevier Academic Press, USA, 2008.
- [20] J. B. MacQueen (1967): Some Methods for classification and Analysis of Multivariate Observations, *Proceedings of 5-th Berkeley Symposium on Mathematical Statistics and Probability*, Berkeley, University of California Press, 1: p. 281-297.
- [21] J. C. Dunn, A fuzzy relative of the ISODATA process and its use in detecting compact well-separated clusters. *J. Cybernetics*, 1973. 3: p. 32-57.
- [22] Bezdek, J., *Pattern Recognition With Fuzzy Objective Function Algorithms*. Plenum Press, New York, 1981 .
- [23] Zadeh, L. A., Fuzzy sets. *Information Control*, 1965. 8: p. 338–353.

- [24] Pedrycz, W., Knowledge-Based Clustering: From Data to Information Granules. J.Wiley & Son Inc., Holboken, USA, 2005.
- [25] Bezdek, J., Fuzzy Mathematics in Pattern Classification PhD thesis Applied Math. Center, Cornell University, Ithaca, USA, 1973.
- [26] Hammersley, J. M. and Clifford, P., Markov field on finite graphs and lattices. 1971, unpublished.
- [27] Besag, J., Spatial interaction and the statistical analysis of lattice systems (with discussions). *Journal of the Royal Statistical Society, 1974. Series B*, 36(2): p. 192-236.
- [28] Grenander, U., *Tutorials in Pattern synthesis*. Brown University, Division of Applied Mathematics, 1983.
- [29] Geman, S. and Geman, D. , Stochastic relaxation, Gibbs distribution and the Bayesian restoration of images. *IEEE Transactions on Pattern Analysis and Machine Intelligence*, 1984. 6(6): p. 721-741.
- [30] Gidas, B., A renormalization group approach to image processing problems. *IEEE Transactions on Pattern Analysis and Machine Intelligence*, 1989. 11: p. 164-180.
- [31] S. Z. Li, Markov Random Field Modeling in Computer Vision, 2001).
- [32] N. Metropolis, A. Rosenbluth, M. Rosenbluth, A. Teller and E. Teller, Equation of State Calculations by Fast Computing Machines. *J. Chem. Phys.*, 1953. 21(6): p. 1087-1092.
- [33] S. Kirkpatrick, C. D. Gelatt Jr. and M. P. Vecchi, Optimisation by Simulated Annealing. *Science*, 1982. 220(4598): p. 671-680.
- [34] Gabor D., Theory of communication J.Inst. Elect. Eng (London), 1946. 93(III): p.429-457.
- [35] Grossmann and Morlet J., Decomposition of Hardy functions into square integrable wavelets of constant shape. *SIAM J. Math.*, 1984. 15: p. 723-736.
- [36] Daubechies I., Orthogonal bases of compactly supported wavelets. *Comm. Pure Appl. Math.*, 1988. 41: p. 909-996.

- [37] Daubechies I., The wavelet transform, time-frequency localization and signal analysis. *IEEE Trans. Inform. Theory*, 1990. IT-36: p. 961-1005.
- [38] Daubechies I., *Ten Lectures on Wavelets*, Philadelphia: SIAM, 1992.
- [39] Mallat S.G., A theory for multiresolution signal decomposition: the wavelet representation. *IEEE Trans. Pattern Anal. and Machine Intell.*, 1989. PAMI-11: p. 674-693.
- [40] Mallat S.G., Multiresolution approximations and wavelet orthogonal bases of $L_2(\mathbb{R})$. *Trans. Amer. Math. Soc.*, 1989. 315: p. 69-87.
- [41] Mallat S.G., Multifrequency channel decomposition of images and wavelet models. *IEEE Trans Acoust. Speech and Signal Proc.*, 1989. ASSP-37: p. 2091-2110.
- [42] J.L. Sanz, R.B. Barreiro, L. Cayon, E. Martinez-Gonzalez, G.A. Ruiz, F.J. Diaz, F. Argueso, J. Silk, and L. Toffolatti, Analysis of CMB maps with 2D wavelets. *Astronomy & astrophysics supplement series*, 1999. 140: p. 99-105.
- [43] S. Tanimoto, G. Rodriguez-Granillo, P. Barlis, S. de Winter, N. Bruining, R. Hamers, M. Knappen, S. Verheye, P. W. Serruys, and E. Regar, A novel approach for quantitative analysis of intracoronary optical coherence tomography: High inter-observer agreement with computer-assisted contour detection. *Cathet. Cardiovasc. Intervent*, 2008. 72: p. 228–235.
- [44] R. Hamers, N. Bruining, M. Knook, M. Sabate, and J. R. T. C. Roelandt, A novel approach to quantitative analysis of intra vascular ultrasound images. *Comput. Cardiol*, 2001. p. 589–592.
- [45] J. M. Bland and D. G. Altman, Statistical methods for assessing agreement between two methods of clinical measurement. *Lancet*, 1986. 1: p. 307–310.
- [46] K. Sihan, C. Botka, F. Post, S. de Winter, E. Regar, R. Hamers, and N. Bruining, A novel approach to quantitative analysis of intravascular optical coherence tomography imaging. *Comput. Cardiol*, 2008 . p. 1089–1092.
- [47] J. Canny, A computational approach to edge detection. *IEEE Trans. Pattern Anal. Mach. Intell.*, 1986. 8: p. 679–698.

- [48] G. T. Bonnema, K. O. Cardinal, S. K. Williams, and J. K. Barton, An automatic algorithm for detecting stent endothelialization from volumetric optical coherence tomography datasets. *Phys. Med. Biol.*, 2008. 53: p. 3083–3098.
- [49] S. Gurmeric, G. Unal, S. Carlier, Y. Yang, and G. Slabaugh, Automatic stent implant follow-up in intravascular optical coherence tomography images. *MICCAI-CVII: The International Workshop on Computer Vision for Intravascular Imaging*, 2008.
- [50] C. Kauffmann, P. Motreff, and L. Sarry, In vivo supervised analysis of stent reendothelialization from optical coherence tomography. *IEEE Trans. Med. Imaging*, 2010. 29: p. 807–818.
- [51] N. Otsu, A threshold selection method from gray-level histograms. *IEEE Trans. Syst. Man. Cybern*, 1979. 9: p. 62–66.
- [52] G. Unal, S. Gurmeric, and S. G. Carlier, Stent implant follow-up in intravascular optical coherence tomography images. *Int. J Cardiovasc. Imaging*, 2010. 26: p. 809–816.
- [53] Bruining N., Sihan K., Ligthart J., de Winter S., Regar E., Automated three-dimensional detection of intracoronary stent struts in optical coherence tomography images. *Computing in Cardiology*, 2011.
- [54] Stavros Tsantis, George C. Kagadis, Konstantinos Katsanos, Dimitris Karnabatidis, George Bourantas and George C. Nikiforidis, Automatic vessel lumen segmentation and stent strut detection in intravascular optical coherence tomography. *Med. Phys.*, 2012. 39(1): p. 503-513
- [55] Hong Lu, Madhusudhana Gargasha, Zhao Wang, Daniel Chamie, Guilherme F. Attizzani, Tomoaki Kanaya, Soumya Ray, Marco A. Costa, Andrew M. Rollins, Hiram G. Bezerra, and David L. Wilson. ' Automatic stent detection in intravascular OCT images using bagged decision trees' *Biomed Opt Express*, 2012. 3(11): p. 2809–2824.
- [56] T. Okamura, N. Gonzalo, J. L. Gutierrez-Chico, P. W. Serruys, N. Bruining, S. de Winter, J. Dijkstra, K. H. Comossaris, R. J. van Geuns, G. van Soest, J. Ligthart, and E. Regar, Reproducibility of coronary Fourier domain optical coherence tomography:

Quantitative analysis of in vivo stented coronary arteries using three different software packages. *EuroIntervention*, 2010. 6: p. 371–379.

[57] F. Prati, E. Regar, G. S. Mintz, E. Arbustini, C. Di Mario, I. K. Jang, T. Akasaka, M. Costa, G. Guagliumi, E. Grube, Y. Ozaki, F. Pinto, and P. W. Serruys, Expert review document on methodology, terminology, and clinical applications of optical coherence tomography: Physical principles, methodology of image acquisition, and clinical application for assessment of coronary arteries and atherosclerosis. *Eur. Heart J*, 2010. 31: p. 401–415.

[58] D. Karnabatidis, K. Katsanos, I. Paraskevopoulos, A. Diamantopoulos, S. Spiliopoulos, and D. Siablis, Frequency-domain intravascular optical coherence tomography of the femoropopliteal artery. *Cardiovasc. Intervent. Radiol.*, 2010. 34: p. 1172–1181.

[59] Bruce F. Torrence, Eve A. Torrence, *The Student's Introduction to Mathematica: A Handbook for Precalculus, Calculus, and Linear Algebra*. Cambridge University Press, 1999.

[60] S. Mallat and S. Zhong, Characterization of signals from multiscale edges. *IEEE Trans. Pattern Anal. Mach. Intell.*, 1992. 14: p. 710–732.

[61] R. Brinks, On the convergence of derivatives of B-splines to derivatives of the Gaussian function. *Comput. Appl. Math*, 2008. 27: p. 79–92.

[62] M. A. Kupinski and M. L. Giger, Automated seeded lesion segmentation on digital mammograms. *IEEE Trans. Med. Imaging*, 1998. 17: p. 510–517.

[63] G. Taubin. Estimation of planar curves, surfaces and nonplanar space curves defined by implicit equations, with applications to edge and range image segmentation. *IEEE Trans. Pattern Analysis Machine Intelligence*, 1991. 13: p. 1115–1138.

[64] W. Gander, G. H. Golub, and R. Strebler. Least squares fitting of circles and ellipses. *BIT*, 1994. 34: p. 558–578.